RAMAN SPECTROSCOPY STUDIES OF ANTIFERROMAGNETIC $FeCO_3$

A THESIS

Presented to

The Faculty of the Division of Graduate

Studies and Research

by

Douglas Bruce Langille

In Partial Fulfillment

of the Requirements for the Degree

Doctor of Philosophy

in the School of Physics

Georgia Institute of Technology

June, 1974

RAMAN SPECTROSCOPY STUDIES
OF ANTIFERROMAGNETIC $FeCO_3$

Approved:

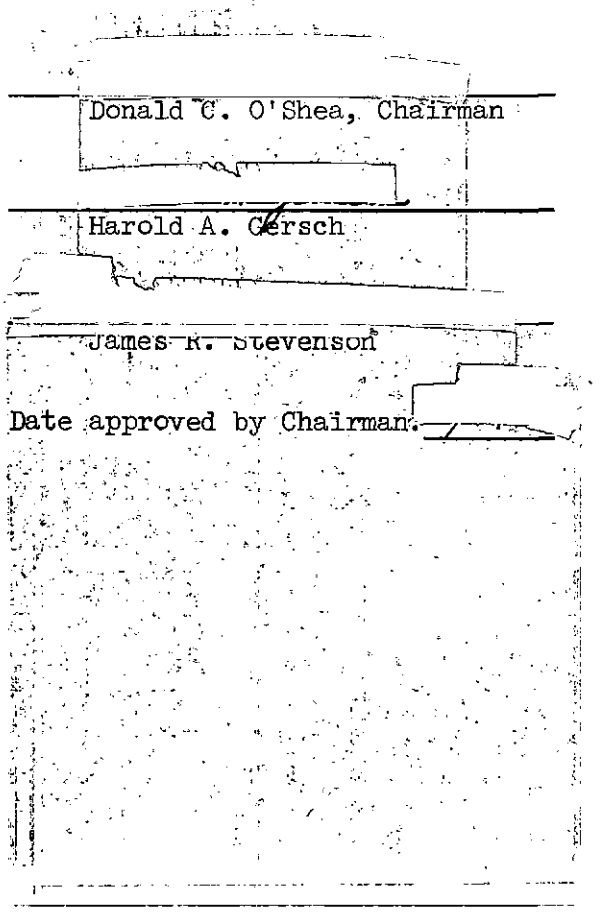

ACKNOWLEDGMENTS

The author wishes to express appreciation to Dr. D. C. O'Shea for his continued guidance and effort as thesis advisor. Thanks is also extended to Drs. H. A. Gersch and J. R. Stevenson for guidance over the author's graduate career and for serving on the reading committee. The author also acknowledges helpful discussions with Dr. S. Spooner.

Special thanks is extended to Mr. R. F. Altman and Mr. J. W. Lynn for assistance in the neutron diffraction experiments. The author is also grateful to two groups of the Georgia Tech Engineering Experiment Station: to Dr. R. A. Young and the Crystal Physics Branch for performing infrared absorption and x-ray diffraction experiments and to the staff of the Analytic Instrumentation Laboratories for impurity analyses of the samples.

The author also appreciates the fellowship provided by the United States Steel Corporation during a portion of this research.

TABLE OF CONTENTS

TABLE OF CONTENTS (Continued)

LIST OF TABLES

LIST OF ILLUSTRATIONS

LIST OF ILLUSTRATIONS (Continued)

SUMMARY

Siderite (natural $FeCO_3$) is a magnetic crystal that undergoes a transition from a paramagnetic phase to an antiferromagnetic phase as the temperature is lowered through 38^oK (the Néel temperature, T_N). Below T_N, the system is considered to have Ising character with the spins oriented exactly antiparallel and only interacting with adjacent spins.

The energy levels of the Fe^{2+} ion are split by a trigonal crystal field and a spin-orbit interaction. Below T_N, the levels are split further by the exchange interaction due to magnetic ordering. However, since the orbital angular momentum is not quenched, the Heisenberg form of the exchange interaction is not expected to apply.

Energies of transitions between the split levels of the Fe^{2+} ions can be measured by the excitations due to the spin-Raman effect of laser light scattering. The effect of magnetic ordering on these levels as the temperature is decreased may be observed by shifts in these energies. Also a study of the vibrational modes of the $FeCO_3$ unit cell at variable temperatures by the Raman effect may give further information about the magnetic ordering.

In addition to the expected vibrational modes, three Raman transitions with temperature dependent frequencies (440, 1175, and 1225 cm^{-1} at 6^oK) were observed and considered to be the transitions between trigonal crystal field and spin-orbit split states (of E_g and A_{1g} symmetry) predicted by theory. However, the observed unequal spacing of the spin-orbit

states of the ground trigonal E_g state is in disagreement with the proposed equal splitting. Sharp decreases in the excitation energies immediately below $38^{o}K$ indicated that the exchange interaction was not of the Heisenberg form. Also observed was an excitation of 741 cm^{-1} considered to be an infrared mode which becomes Raman active. The intensity of this line increases with decreasing temperature possibly due to a loss of inversion symmetry as a result of Fe^{2+} ion ordering. The persistence of this line as a shoulder on a Raman active line at room temperature indicates that short range magnetic order may persist to $300^{o}K$.

CHAPTER I

INTRODUCTION

For many years there has been considerable interest among researchers in the field of solid state physics in antiferromagnetic systems. In these systems the electron spins of the adjacent magnetic ions in a sample orient in approximately opposite directions resulting in a magnetic ordering but no magnetic field in the sample. The electron spins are not oriented at all temperatures but undergo a transition from generally random orientation in a paramagnetic phase to an oriented antiferromagnetic phase as the temperature is decreased through the Néel temperature (T_N). In Ising systems, the orientation is due to only the interaction of nearest neighbor spins and the spins are oriented exactly antiparallel. Ferrous carbonate is an antiferromagnetic system with Ising character and a Néel temperature of $38^{o}K$.

The Exchange Interaction and Orbital Angular Momentum

The description of the behavior of the ions in an ordered state is expressed in terms of the exchange interaction. The simplest example of the exchange interaction is in the removal of degeneracy of interchange in a two electron system when the Coulomb interaction, V_{12}, between the two electrons is considered. The resultant level splitting is $\pm J_{12}$, where

$$J_{12} = \int \psi_k(\bar{r}_1)\psi_m(\bar{r}_2)V_{12}\psi_k(\bar{r}_2)\psi_m(\bar{r}_1)dv_1dv_2 \qquad (1)$$

is the exchange integral and $\psi_k(\bar{r}_1)$ is the solution of the Schrodinger equation for electron 1 in the state k, etc. With consideration of the requirement of the Pauli exclusion principle that only antisymmetric wave functions be used, the same interaction can be expressed with respect to the spin angular momentum operators, $\bar{S}_1$ and $\bar{S}_2$, of the two electrons as

$$-2(J_{12}\bar{S}_1\cdot\bar{S}_2 + \frac{1}{4}), \qquad (2)$$

which is Heisenberg form of the exchange interaction. Although this form resembles a strong direct coupling between the spins, the splitting is a result of the exclusion principle requiring one type of orbital solution when the spins are parallel and another when they are antiparallel.[1] The extension of the Heisenberg form of the exchange interaction to the case of electrons in crystals will be discussed after the effects of the crystal on the ion are considered.

In the case of a free ion, the electrons move in the single electron orbits of a spherical symmetric Coulomb potential resulting in an orbital angular momentum, $\bar{L}$, for the entire ion. When the spin, $\bar{S}$, resulting from the single electron spins is considered, the free ion state is $(2L + 1) \cdot (2S + 1)$-fold degenerate. However, when the ion is in a crystalline environment, it experiences an electrostatic field imposed by the surrounding ions, causing a distortion in the orbits of the electrons outside closed shells. The orbital degeneracy is partially removed by a splitting of the free ion level into several levels each

with a symmetry corresponding to a representation of the group of the crystal field. The wavefunctions of each level are combinations of the free ion wavefunctions, and the ground level (with the highest population) will have an orbital angular momentum (different from the free ion case) determined from the expectation value with respect to the new ground state wavefunctions.

Also to be considered is the interaction of the electron's orbital motion with its spin (the spin-orbit interaction). The interaction is fully expressed by the relativistic Dirac equation[2] but the term considered in the case of electrons in crystals is

$$\frac{\hbar}{4m^2c^2} \nabla V \times \bar{p} \cdot \bar{s} \tag{3}$$

where V is the potential of the electron (due principally to the nucleus and the crystal field).[3] If V were spherically symmetric, the form of the interaction would reduce to

$$\left(\frac{\hbar}{4m^2c^2} \frac{1}{r} \frac{\partial V}{\partial r} \right) \bar{L} \cdot \bar{S} \tag{4}$$

where the matrix element of the factor in parenthesis with respect to free ion wave functions is usually taken to be a constant. This interaction results in further splitting of the ion accompanied by a partial removal of the spin degeneracy. In the case of transition metal ions the spin-orbit splitting is smaller than the crystal field splitting.

If there are still degenerate levels there can be further splitting that is due to the exchange interaction between the ions in the crystal.

In an extension of the two electron to that of multi-electron systems in crystals, the Pauli exclusion principle requires that the wave functions representing the electrons in the crystal be antisymmetric if both the spin and orbital coordinates of any two electrons be interchanged. In the special case in which the free ion was in a pure $\overline{S}$ state ($L = 0$), the Heisenberg form would apply since the crystal field would not effect these orbital states. Even in the case of non-zero orbital angular momentum ($\overline{L} \neq 0$) in the free ion state, the Heisenberg form may be used if the orbital angular momentum is quenched in the crystal. Quenching will occur if the crystal field potential is sufficiently asymmetric so that no axis of symmetry remains about which the orbital angular momentum is conserved. L will be effectively zero and a pure $\overline{S}$ state will be assumed. However, when the orbital angular momentum is not quenched, the orbital motion of the electrons which is distorted from free ion motion by the crystal field will have to be considered. Since the free single electron wavefunctions which are used in the exchange integrals (such as (1) in the two electron case) do not apply, the exchange interaction would not be of the Heisenberg form.[4] In the case of $FeCO_3$, an unquenched $\overline{L}$ persists in the crystal field and the Heisenberg form would not be expected to apply.

The Siderite System

$FeCO_3$ was studied in this research mainly in its natural crystal form, siderite. The crystal structure of siderite is rhombohedral, belonging to the D^6_{3d} ($R\ \overline{3}\ C$) space group. As shown in Figure 1, the unit cell contains 10 atoms; the carbonate ions lie in the basal plane and each successive carbonate ion along the C-axis is rotated 180^o. The crystal

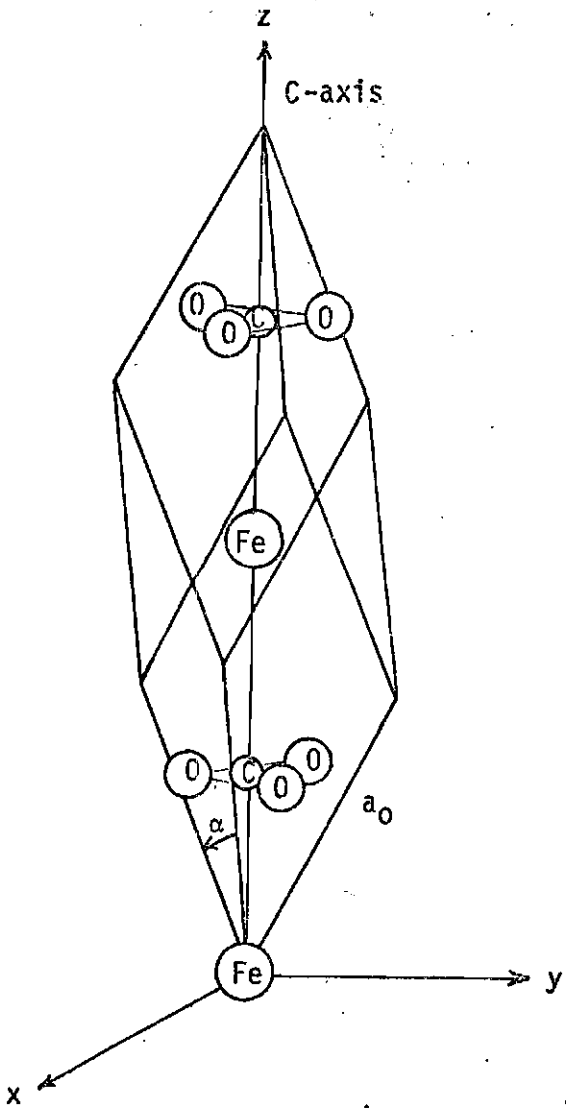

Figure 1. Unit Cell of Iron Carbonate.

parameters a_o and α are 5.795 Å and $47^o45'$, respectively, with a carbon-oxygen distance of 1.23Å.[5] Below the Neel temperature (38^oK), the ferrous ion spins order antiferromagnetically parallel to the C-axis in alternating basal plane ferromagnetic sheets.

Previous Research on $FeCO_3$

Several experiments have been performed which establish the antiferromagnetic nature and Ising character of siderite. Neutron diffraction experiments of Alikhanov[6] established an antiferromagnetic structure by the appearance of an additional (100) reflection at liquid hydrogen temperature (20.4^oK). The absence of a (111) reflection indicated that the spins were directed along the C-axis. Temperature dependence of the (100) reflection revealed a transition temperature of approximately 35^oK.

Measurements of Jacobs[7] present further demonstration of a predominantly antiferromagnetic system with large anisotropy. Susceptibility measurements indicate a Neel point (T_N) at approximately 38^oK. Also, the ratio of parallel to perpendicular susceptibilities (with respect to the C-axis) of 8.8 at T_N indicates a very large anisotropy with the spins oriented parallel to the C-axis. Magnetization curves at 4.2^oK indicate a transition by spin-flipping to a ferromagnetic state which is nearly completed at 200 kO_e with about $6\mu_B$ per ferrous ion (a value which exceeds the expected value if only spins contribute to the magnetic moment). Fair agreement with magnetization curves is obtained by assuming only antiferromagnetic interaction between nearest neighbor ions.

Mössbauer data provide information pertaining to the antiferromagnetic transition. From theoretical spectra of $FeCO_3$ in close agreement with experimental spectra between 4.65°K and 38.1°K, Forester and Koon[8] obtained the temperature of the degree of magnetic order (or the order parameter $\eta(T)$). This temperature dependence was in agreement with the form of $\eta(T)$ for a highly anisotropic Ising-like magnetic system,

$$\eta(T) = D\left(\frac{T_N - T}{T}\right)^B \qquad (5)$$

where B = .3185 for the $FeCO_3$ system[9] (compared with B = .312 for a three dimensional simple cubic lattice Ising model).

Other previous research is related to the energy level splitting of the Fe^{2+} ion. A cubic field causes the largest splitting (10,000 cm^{-1}) followed by a splitting due to a trigonal distortion from cubic symmetry. A ground Eg doublet and A_{1g} singlet (separated by 1,000 cm^{-1}) are the two lowest levels in the trigonal field.[10] By taking the ratio of the quadrupole splitting in $FeCO_3$[11] (obtained from Mössbauer data) to the splitting in $FeSiF_6 \cdot 6H_2O$[12], the proportion of mixing of the free ion wave functions in the trigonal ground state were determined by Okiji and Kanamori.[13] By evaluating the expectation value of L with respect to these wave functions, values of $\langle L_z \rangle = 1$ and $\langle L_x \rangle = \langle L_y \rangle = 0$ for the time average of the spatial components of the orbital angular momentum were obtained.

There is further splitting of the trigonal ground state into five doubly degenerate Eg states and perhaps the A_{1g} state into five non-degenerate levels. These states are split by the exchange interaction below the Néel temperature. An excitation of approximately 112 cm^{-1} between

the two lowest spin-orbit states after they are exchange split has been observed below 38°K, by two different experiments: neutron diffraction by Wrege et al.[14] and infrared absorption by Prinz and Forester.[15] Prinz and Forester consider the exchange interaction to be due to the spins alone while Wrege et al. add an orbital angular momentum value of $L_Z = 1$ directly to the spin. The choice of the form of the exchange interaction was flexible in these cases since only one transition was being considered. The form may need to be more definite if more transitions between other spin-orbit exchange split states are to be accounted for.

Investigation of $FeCO_3$ by Raman Spectroscopy

The Raman effect involves a shift in frequency of light scattered from the system studied. The most common excitation in crystals causing this shift are optical vibrational modes of the atoms in the unit cell. Also observed in paramagnetic systems are transitions between electronic split levels via coupling of the light with the spins.

In $FeCO_3$ transitions between the trigonal spin-orbit split Fe^{2+} states could be observed to the higher lying Eg spin-orbit split states and the A_{1g} states. This would provide the first experimental values for these splittings to test the various forms for the crystal field and spin-orbit interactions. Studying these transitions as the temperature is decreased through $T_N = 38°K$ would investigate the effect of the exchange interaction on these levels and test forms of the exchange interaction.

Also, a study of the vibrational modes as the temperature is decreased may provide further information on the effects of ordering on the crystal.

CHAPTER II

THEORY

Classical Theory of the Raman Effect for Vibrational Excitations

For the particular case of vibrational excitations, the Raman effect is explained classically by the change of polarizability during the specific vibration. The electric field of the incident light, $\overline{E}$, the induced cipole moment in the system, $\overline{M}$, and the polarization tensor α are related by

$$\begin{aligned} M_x &= \alpha_{xx}E_x + \alpha_{xy}E_y + \alpha_{xz}E_z \\ M_y &= \alpha_{yx}E_x + \alpha_{yy}E_y + \alpha_{yz}E_z \\ M_z &= \alpha_{zx}E_x + \alpha_{zy}E_y + \alpha_{zz}E_z \end{aligned} \tag{6}$$

For vibrations of small amplitude α_{xx} may be expanded as

$$\alpha_{xx} = \alpha_{xx}^{0} + \sum_i \left(\frac{\partial \alpha_{xx}}{\partial Q_i}\right)_o Q_i + \sum_{i,j} \frac{\partial \alpha_{xx}}{\partial Q_i \partial Q_j} Q_i Q_j + \ldots \tag{7}$$

where Q's are normal coordinates given by

$$Q_i = Q_i^{o} \cos 2\pi \nu_i t \ . \tag{8}$$

If the incident radiation has frequency ν, the vibrating electric vectors are expressed as:

$$E_x = E_x^o \cos 2\pi\nu t$$
$$E_y = E_y^o \cos 2\pi\nu t \qquad (9)$$
$$E_z = E_z^o \cos 2\pi\nu t$$

Then the X component of the induced dipole moment is

$$M_x = (\alpha_{xx}^o E_x^o + \alpha_{xy}^o E_y^o + \alpha_{xz} E_z^o) \cos 2\pi\nu t$$
$$+ \sum_i \left[\left(\frac{\partial \alpha_{xx}}{\partial Q_i}\right)_o E_x^o + \left(\frac{\partial \alpha_{xy}}{\partial Q_i}\right)_o E_y^o + \left(\frac{\partial \alpha_{xz}}{\partial Q_i}\right)_o E_z^o \right] Q_i^o \times$$
$$\frac{1}{2} [\cos 2\pi(\nu + \nu_i)t + \cos 2\pi(\nu - \nu_i)t] + \ldots \qquad (10)$$

and similarly for M_y and M_z. It is the second term with frequencies $\nu \pm \nu_i$ which leads to the Raman scattering. Hence for a vibration to be Raman active, it is necessary that at least one of the components $\left(\frac{\partial \alpha_{xx}}{\partial Q_i}\right)_o$,..., does not vanish.

An expression for second-order Raman scattering is obtained by including the third term in (7). A typical result (arising from the $\alpha_{xx}E_x$ term) is

$$\frac{1}{4} \sum_{i,j} \frac{\partial \alpha_{xx}}{\partial Q_i \partial Q_j} E_x^o Q_i^o Q_j^o \; [\cos 2\pi(\nu + \nu_i + \nu_j)t + \cos 2\pi(\nu + \nu_i - \nu_j)t$$
$$+ \cos 2\pi(\nu - \nu_i + \nu_j)t + \cos 2\,(\nu - \nu_i - \nu_j)t] \; .$$

Here new frequencies $\nu_i \pm \nu_j$ arise as combinations of first order frequencies. If i = j, the resulting combination is an overtone.[16]

Quantum Theory of Vibrational Raman Effect and Infrared Absorption in Molecules

Quantum mechanically, Raman excitations are considered to be two

virtual electric dipole transitions from a ground state, i, to intermediate states, I, and then from I down to a final state, f. The electric field of the incident light of frequency can be expressed as

$$\bar{E} = \bar{A}^* e^{2\pi i\gamma t} + A e^{-2\pi i\gamma t} \tag{12}$$

where A is a complex vector. In the case of molecules, the intensity of scattered radiation per molecule is

$$I_{kn} = \frac{64\pi^4(\nu + \nu_{if})^4}{3c^3} |\bar{E}_{if}|^2 \tag{13}$$

where

$$E_{if} = \frac{1}{h} \sum_I \frac{(\bar{A}M_{iI})M_{If}}{\nu_{Ii} - \nu} + \frac{M_{iI}(\bar{A}M_{If})}{\nu_{If} + \nu} \tag{14}$$

and M is the matrix element for the electric moment between the indicated states (for example,

$$M_{iI} = \int \phi_I^* \sum_j \xi_j \phi_i \, d\tau \tag{15}$$

where the sum is over outer electrons of the atoms).

From equation (9), a tensor relationship between A and E_{if} can be obtained. For the x-component

$$(E_x)_{if} = \sum_{j=x,y,z} (\beta_{xj})_{if} A_j \tag{16}$$

where

$$(\beta_{xj})_{if} = \frac{1}{h} \sum_{I} \frac{(M_j)_{iI}(M_x)_{in}}{\nu_{Ii} - \nu} + \frac{(M_x)_{iI}(M_j)_{If}}{\nu_{If} + \nu} \qquad (17)$$

is the scattering tensor.

It is sometimes possible to express the scattering tensor in terms of the wave functions of the nuclear motion and the polarizability of the molecule to avoid performing a summation over excited electronic states. In the case where the atomic nuclei move much more slowly than the electrons, the adiabatic approximation can be made. In this approximation, the wave function of the molecule, $\psi(\epsilon,x)$, can be written as a product of the electronic function, $\phi(\epsilon,x)$, and the nuclear function, $u(x)$:

$$\psi_{nv}(\epsilon,x) = \phi_n(\epsilon,x)u_{nv}(x) \qquad (18)$$

where ϵ is the set of all the electronic coordinates, x is the set of all nuclear coordinates and n and v are the corresponding quantum numbers. By using ψ_{nv} in the matrix elements $(M_j)_{iI}$, $(M_x)_{in}$, etc., of equation (12), the scattering can be expressed in terms of the polarizability tensor α_{xj} and the nuclear functions:

$$(\beta_{xj})_{if} = \int u^*_{n_1 v_k}(x)\alpha_{xj}(x)u_{n_1 v_1}(x)dx \qquad (19)$$

Equation (14) is valid when the exciting frequency, ν, is far from the electron absorption frequency, ν_{Ii}. Resonance Raman scattering will occur when ν is close to ν_{Ii} and the scattering tensor in equation (17) will be enhanced due to the resonant denominator.

A Raman transition from k to n is allowed if at least one of the

six quantities $(\beta_{xx})_{if}$, $(\beta_{xy})_{if}$ ... is different from zero, or if the product $\psi_k\psi_n^*$ has the same symmetry type as at least one of the (α_{xx}), (α_{xy}), ...

The components of the polarizibility tensor transform under symmetry operations as do the products of the corresponding vectors. The vectors transform as

$$\begin{aligned} Rx &= x \cos\phi + y \sin\phi \\ Ry &= -x \sin\phi + y \cos\phi \\ Rz &= \pm z \end{aligned} \tag{20}$$

where the + or - sign corresponds to the operation R being a pure rotation or a rotatory reflection (rotation followed by a reflection through the z = 0 plane) about the z axis through an angle ϕ. Therefore the corresponding transformation equations of the components of the polarizability tensor are:

$$\begin{aligned} R_{\alpha_{xx}} &= \alpha_{xx} \cos^2\phi + \alpha_{yy} \sin^2\phi + \alpha_{xy} \sin^2\phi \\ R_{\alpha_{xy}} &= -\frac{1}{2}(\alpha_{xx} - \alpha_{yy}) \sin\phi + \alpha_{xy} \cos^2\phi, \\ R_{\alpha_{xz}} &= \pm \alpha_{xz} \cos\phi \pm \alpha_{yz} \sin\phi \\ R_{\alpha_{zz}} &= \alpha_{zz} \, . \end{aligned} \tag{21}$$

If the representation of this tensor contains the irreducible representation $\psi_k\psi_n^*$, then at least one of the products $\alpha_{xx}\psi_k\psi_n^*$, $\alpha_{xy}\psi_k\psi_n^*$ will be invariant and the transition will be allowed in the Raman effect.

If the sum of the diagonal elements of the representation of the operation R (or character) is known, the Raman active vibrations can be determined. The character in the reducible representation of the polarizability tensor is

$$\chi_\alpha (R) = 2 \cos \phi \ (\pm 1 + 2 \cos \phi) \ , \tag{22}$$

where the - sign is applied for a rotary reflection. The number of times the character, $\chi_i(R)$, of a vibration symmetry appears in the $\chi_\alpha(R)$ is

$$N_i = \frac{1}{N_G} \sum n \chi_\alpha(R) \chi_i(R) \tag{23}$$

where N_G is the number of elements in the group, n is number of elements in each class and the summation extends over all the classes of the group. If N_i is not zero, the vibrations are Raman active.

In the case of infrared absorption, there is a direct dipole transition from k to n. In the above discussion the polarizability tensor would be replaced with the electric dipole operator $e \bar{r}$ having the vector transformation properties of (20). The character then becomes

$$\chi_M(R) = \pm 1 + 2 \cos \phi \tag{24}$$

with

$$N_M = \frac{1}{N_G} \sum n \chi_M(R) \chi_i(R) \tag{25}$$

as the number of times $\chi_i(R)$ of a vibration appears in $\chi_M(R)$.

However, the actual number of vibrations of each depends on the number of atoms in the molecule. This is calculated as

$$N = \frac{1}{N_G} \sum n \chi(R) \chi_i(R) \tag{26}$$

where

$$\begin{aligned} \chi(R) &= (u-2)(1+2\cos\phi) \quad \text{for rotations} \\ &= u(-1+2\cos\phi) \quad \text{for rotatory reflections,} \end{aligned} \tag{27}$$

and u is the number of atoms unchanged by the operation R.[16]

The Raman Effect in Crystals

The Raman effect in crystals is similar to the molecular case. However, in the crystal, additional excitations are possible such as phonons (lattice vibrations), magnons (spin-waves), and transitions between crystal field split electronic states. The following formulation[19] (obtained by application of time-dependent second-order perturbation theory) can be used as a starting point for describing these excitations. From second order time dependent perturbation theory the transition probability per unit volume per unit time is given by

$$W_{if} = \frac{2\pi}{h} N |K|^2 \rho_E \tag{28}$$

where

$$K = \sum_{I} \left[\frac{\langle f,(n-1)_{k_o},(n+1)_{k_s} | \sum_{b} H^{b}_{er}(\bar{k}_s,\omega_s) | I,(n-1)_{k_o},n_{k_s} \rangle \langle I,(n-1)_{k_o},n_{k_s} | \sum_{b} H^{b}_{er}(\bar{k}_o,\omega_o) | i,n_{k_o},n_{k_s} \rangle}{\hbar(\omega_o - \omega_{Ii})} \right.$$

$$\left. - \frac{\langle f,(n-1)_{k_o},(n+1)_{k_s} | \sum_{b} H^{b}_{er}(\bar{k}_o,\omega_o) | I,n_{k_o},(n+1)_{k_s} \rangle \langle I,n_{k_o},(n+1)_{k_s} | \sum_{b} H^{b}_{er}(\bar{k}_s,\omega_s) | i,n_{k_o},n_{k_s} \rangle}{\hbar(\omega_s + \omega_{Ii})} \right]$$

(29)

with

$$\rho_E = k_s^2 \; \delta(\hbar\omega_o + E_i - \hbar\omega_s - E_f) d\Omega \; d\omega_s/(2\pi)^2 \; c\hbar \qquad (30)$$

$$\omega = \omega_s + \omega_{fi}$$

In these expressions, i, I and f refer to the initial, intermediate and final states, of the particular excitation, n_{k_o} and n_{k_s} are the initial numbers of photons in the incident (k_o) and scattered (k_s) modes and N is the number of unit cells per unit volume. The interaction H^k_{er} between the radiation field and the b^{th} atom in the unit cell, becomes in the electric-dipole approximation

$$H^k_{er}(k,\omega) = -e \, \bar{r}_b \cdot \bar{E}_b(k,\omega) \qquad (31)$$

where the sum over electrons has been indicated by repeated indices.

For the one phonon scattering process $|i\rangle = |G, n_q\rangle$ and $|f\rangle = |G,(n+1)\rangle_q$ with $|G\rangle = \prod_b |g\rangle_b$, where $|g\rangle_b$ is the ground electronic state of the b^{th} atom, and n_q is the number of phonons with wave vector $q = k_o - k_s$. K would vanish if there were no electron-phonon interaction in the system, since H_{er} cannot connect states with different phonon occupation numbers. With an electron-phonon interaction

$$H_{ep} = \sum_b \sqrt{M} \; \bar{U}_b \cdot \bar{F}_b \qquad (32)$$

operating on both ground and excited states, $|n_q\rangle$ and $|(n+1)_q\rangle$ become mixed (M, U_b and $\bar{F}_b$ are the atomic mass, atomic displacement, and generalized force on the atom, respectively).

If the intermediate states can be written as $\langle I| = \langle (n+1)_q, i|$, then the mixing in the transition from the initial to intermediate states can be written as

$$\langle (n+1)_q, i|e\bar{r}|n_q, g\rangle = \frac{\langle i|e\bar{r}|g\rangle}{\hbar\omega_q}\left[\langle (n+1)_q, i|H_{e-p}|n_q, i\rangle - \langle (n+1)_q, g|H_{e-p}|n_q, g\rangle\right], \tag{33}$$

with a similar expression for the transition from the intermediate state to the final state.

Selection Rules for Crystals

Vibrations in a crystal can be treated in a manner similar to molecular vibrations. The basic difference is that the symmetry of the entire crystal must be considered rather than just the molecular structure which makes up the unit cell. The space group of the crystal may consist of translation operations as well as the point symmetry operations in the molecular case.

There are only two types of combined rotation - translation operations which are not transformable to point group operations. These are known as glide and screw operations. A screw operation consists of a real rotation followed by a translation. A glide consists of a reflection followed by a translation.

The introduction of screw and glide operations effects the selection rules in two ways. First, additional screw or glide operations may be added to the point group operations or some point group operations may be modified to screw or glide operations resulting in additional or

new characters in (22) through (27). Also, there may be a different number of atoms unchanged by an operation in (27).

Polarization Selection Rules

A relationship exists between the polarization tensor components and the orientation of the axes of the molecule or crystal unit cell. Referring to (16)

$$(E_x)_{if} = \sum_{j=x,y,z} (\beta_{xj})_{if} A_j \ , \tag{34}$$

the existence of a particular α_{xj} means that incident light polarized parallel to the j axis will induce a moment parallel to the x axis. The scattered light will in turn be parallel to the x-axis. In the case of oriented crystals, orthogonal axes in an experimental arrangement can be related to symmetry directions of the crystal structure.

The existence of a particular excitation in certain polarization tensor components can be used to identify the symmetry or representation of the excitation. Since the polarization tensor transforms as a product of two vectors, a given tensor component will be active for a particular representation if the corresponding vector component product belongs to that representation. For example, an E_g symmetry mode will be active in the α_{xy} component if the product xy belongs to the E_g representation. The projection operator, p^j

$$p^j = \frac{l_j}{h} \sum_R x^j(R)^* P_R \tag{35}$$

can be used to determine the products that belong to a particular representation, j, where l_j is the dimension of the representation, P_R is the operation of the R^{th} element of the group, h is the number of

elements in the group and $\chi^j(R)$ is the character of the R^{th} element. From an arbitrary function, p^j projects out the part belonging to the j^{th} representation. Therefore, if after operating on a particular vector component product with p^j a non-zero result is obtained, then excitations of the j^{th} representation will be active in the corresponding polarization tensor component.[21]

Vibrational Modes for D_{3d}^6 Symmetry

Ferrous carbonate belongs to the D_{3d}^6 space group which has the following symmetry operations:[20]

(a) one identity operation (E)

(b) two three-fold axes along the c-axis (C_3)

(c) three two-fold axes along the carbon-oxygen direction (C_2)

(d) one inversion operation about the iron atom site (I)

(e) two 60^o rotation-reflection axes along the c axis (S_6). (The reflection being in a plane perpendicular to the c-axis through the iron site.)

(f) three glide planes consisting of reflections in plane containing the c-axis and lines in the basal plane 30^o away from the two-fold axis followed by a translation of half a unit cell along the c-axis.

The atomic arrangement of the unit cell with the symmetry axes labeled is given in Figure 2. The symmetry of the entire crystal can be observed by a projection of a portion of the structure on a plane normal to the three-fold axes and passing through the apex of the cleavage rhombohodren in Figure 3. The distances are fractions of the c-axis length below the plane.

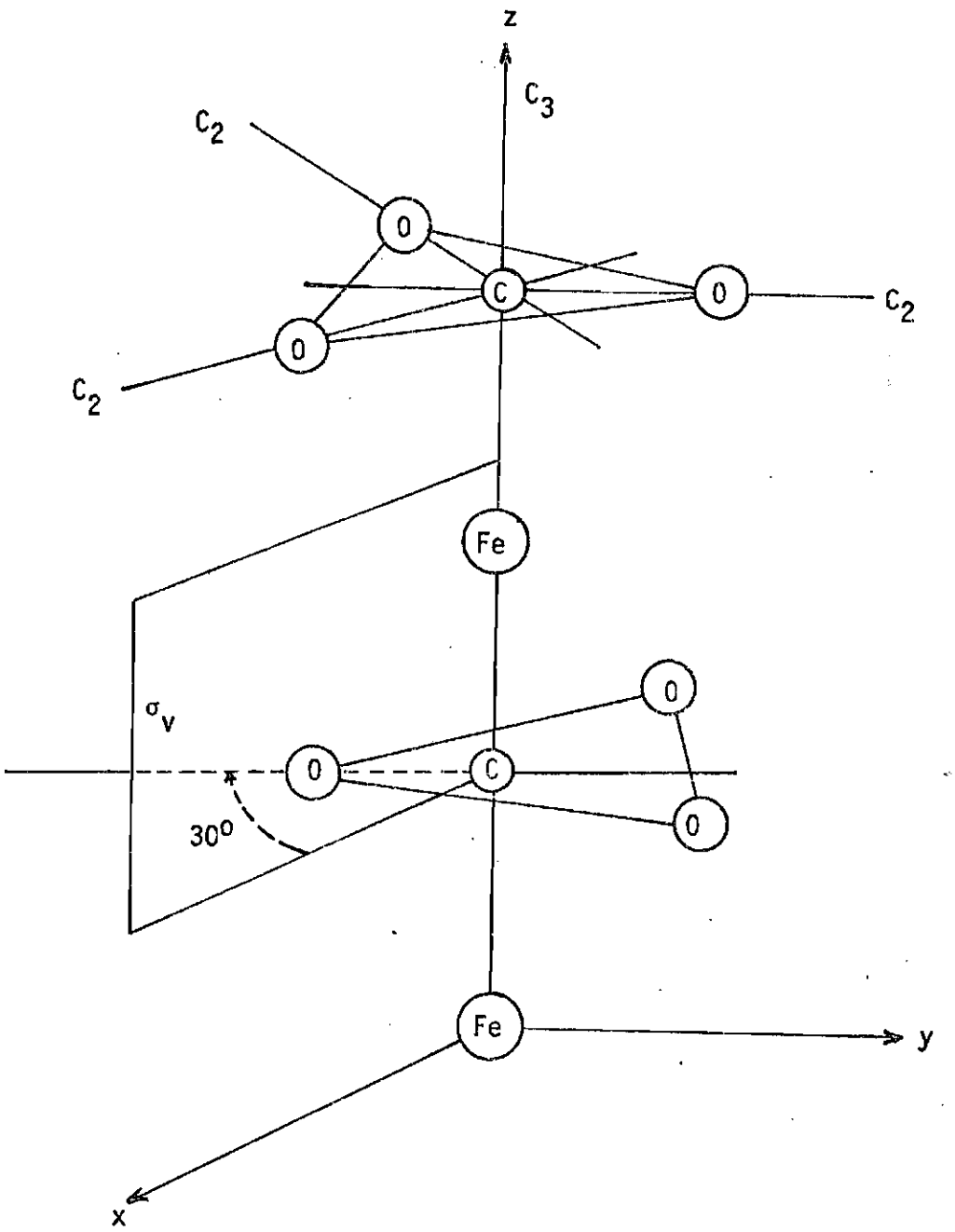

Figure 2. Unit Cell of $FeCO_3$ with Symmetry Operations of D_{3d}^6.

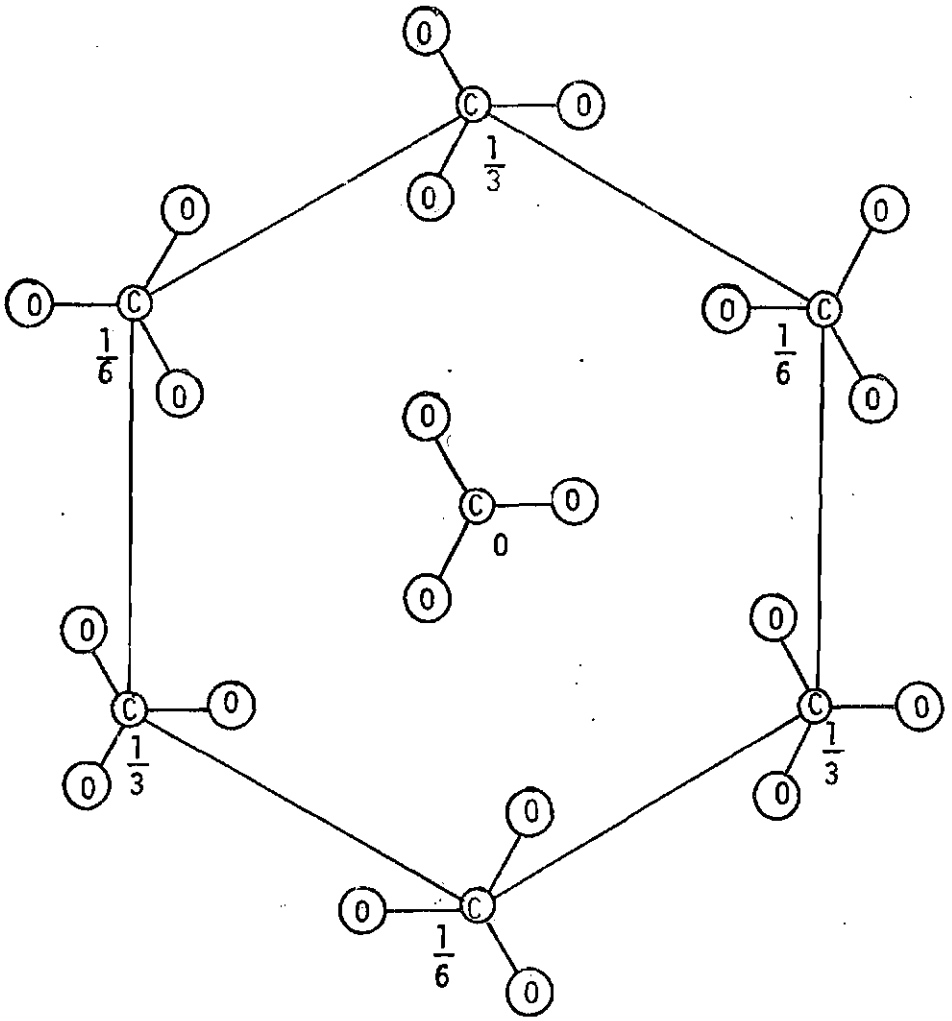

Figure 3. A Projection of the $FeCO_3$ Structure on a Plane Normal to the Threefold Axis.[5] (Only carbonate ions are shown. The Fe depth below the center carbonate is $\frac{1}{4}$.)

The application of equations (22) through (27) to the case of $FeCO_3$ is summarized in Table 1. The result is that there are 1 A_{1g} and 4 E_g Raman active modes, 3 A_{2u} and 5 E_u infrared active modes, and 2 A_{1u} and 3 A_{2g} inactive modes. Of the Raman active modes, the active polarization components are $\alpha_{xx} = \alpha_{yy}, \alpha_{zz}$ for A_{1g} and $\alpha_{xx} = -\alpha_{yy}, \alpha_{xy}, \alpha_{yz}, \alpha_{zx}$ for E_g.

The Two-Phonon Raman Effect in Crystals

The two-phonon Raman effect in crystals may be explained by a direct extension of the first order process. After a photon ω_i is absorbed, two phonons ω' and ω'' are created in a single event, and a photon ω_s is emitted ($\omega_s = \omega_i - \omega' - \omega''$). The scattering crystal is generally in its electronic ground state with all valence bands full and all conduction bands empty at the start of the scattering process, and it returns to its electronic ground state at the end of the event. The virtual intermediate states involve the excitation of electron-hole pairs. The restriction that the sum of the phonon wave vectors equal the change in the scattered photon wavevector combined with the negligible magnitude of the photon wavevectors (compared with Brillouin zone dimensions) requires that the wave vectors of the two phonons should be equal and opposite.

The determination of which two phonon processes are most likely is related to location of critical points on two phonon dispersion curves. The two phonon dispersion curves are constructed by adding together all pairs of single phonon branches at each wavevector k. The critical points on the two phonon dispersion curve occur when the slope, $(\frac{\partial \omega}{\partial k})$, equals zero

Table 1. Summary of Analysis of Vibrational Modes in D^6_{3d} Symmetry[22]

D^6_{3d}		E	$2C_3$	$3C_2$	i	$2S_6$	3σ	N_α	N_m	$N_{vibration}$	Activity	Active Component
Character	A_{1g}	1	1	1	1	1	1	2	0	1	R	$\alpha_{xx} = \alpha_{yy}, \alpha_{zz}$
	A_{1u}	1	1	1	-1	-1	-1	0	0	2	i.a.	
	A_{2g}	1	1	-1	1	1	-1	0	0	3	i.a.	
	A_{2u}	1	1	-1	-1	-1	1	0	1	3	ir	
	E_g	2	-1	0	2	-1	0	2	0	4	R	$\alpha_{xx} = -\alpha_{yy}$ $\alpha_{xy}, \alpha_{yz}, \alpha_{zx}$
	E_u	2	-1	0	-2	1	0	0	1	5	ir	
$\chi_\alpha(R) =$												
$2\cos\phi\ (\pm 1 + 2\cos\phi)$		6	0	2	6	0	2					
$\chi_M(R) = \pm 1 + 2\cos\phi$		3	0	-1	-3	0	1					
$\chi(R) = (u-2)(1+2\cos\phi)$		24	0	-2								
$= u(-1 + 2\cos\phi)$					-6	0	0					

or changes sign discontinuously. At a critical point the density of states will have a discontinuity and hence there will be a higher probability of a two phonon excitation at that point. Most of the critical points occur at points of high symmetry in the Brillouin zone at the center or boundaries.

The polarization selection rules create further specifications on which points on the two-phonon dispersion curve can be Raman active. The symmetry of a point is obtained from the direct product of the representations of the participating single phonons at that point. If the reduction of this direct product contains representations which were first-order Raman active, then the two-phonon excitation will also be active.[22]

Spin-Raman Scattering

Two mechanisms have been proposed for Raman scattering between different spin states. The first, proposed by Bass and Kaganov,[24] considered the spin system to be directly coupled to the radiation field by a magnetic-dipole interaction. However, this interaction lead to a insufficient scattering efficiency and incorrect polarization selection rules in comparison with experimental observation. The other mechanism pointed out by Elliott and Loudon[25] involves two electric-dipole interactions between electronic energy levels as in the phonon and electronic scattering cases. In the spin scattering case the initial and final states must have different spin states and hence a spin-orbit interaction is required to mix these states (similar to the requirement of an electron-phonon interaction in the phonon case).

In the case of the electric dipole mechanism for spin-Raman scattering, equation (29) for the Raman transition probability may be used again. Here the eigenstates are characterized by spin and orbital angular momentum states. The spin part connected with the ground orbital state (which is usually assumed to be quenched) is specified by the magnon occupation number. Using the same notation as in the phonon case, the initial and final states can be written as $|i\rangle = |G,n_q\rangle$ and $|f\rangle = |G,(n+1)_q\rangle$ with $|G\rangle = \prod_b |g\rangle_b$. However, here $|g\rangle$ is the ground orbital state of a magnetic ion and n_q is the number of magnons with wave vector $q = k_o - k_s$ and frequency ω_q. However, since H_{er} cannot change the magnon occupation number, the Raman transition probability would vanish if there were no spin-orbit coupling in the ground and excited states.[18] By considering

$$H_{S-L} = \sum_{m,b} \lambda_{mb} L_{mb} S_{mb} \qquad (36)$$

(where the b^{th} atom is in the m^{th} unit cell) as a perturbation on the intermediate states $|I\rangle$ the states $|n_q\rangle$ and $|(n+1)_q\rangle$ can be mixed, and the transition probability no longer vanishes.[19]

The selection rules for spin-Raman transitions depend on the effects of the crystal field and the orbital angular momentum. In crystals with quenched angular momentum and a small crystal field, $M_s = \pm 1$ is a valid magnetic number selection rule (this requires the polarization condition that the incident field should have right circular polarization around, and the scattered field a linear polarization along the magnetization, or vice versa.) However, these selection rules break down if the

orbital angular momentum is not completely quenched, or if the crystal field is large. In these cases, the states of different M_S will be separated by the spin-orbit interaction and the crystal field. In the case of a spin-orbit interaction, M_J will become a good quantum number and the M_S states will be mixed over the M_J manifold. Therefore in the case of two adjacent (in energy) M_J levels, spin-Raman transitions may occur provided $M_S = 0, \pm 1$, or ± 2.

The effect of unquenched orbital angular momentum produces another distinction in the case of magnetic systems which order below a critical temperature (T_c). If the energy separation between initial and final states is due only to different spin states, the excitation will vanish above T_c. However, if the orbital angular momentum is not quenched and the initial and final spin states are associated with different spin-orbit split states, the excitation between the different spin states will persist above T_c. The existence of spin-Raman scattering in paramagnetic systems is a further example of this.[19]

Energy Level Splitting of Fe^{2+} in $FeCO_3$

The free Fe^{2+} ion (in the $^5D_4$ ground state) with $L = 2$ and $S = 2$ is 25-fold degenerate. In crystalline fields of D_{3d} symmetry the degeneracy of the ion energy levels is partially lifted. The antiferromagnetic Ising nature of $FeCO_3$ causes further splitting. Two splitting schemes have been proposed which differ in the relative strengths considered for the trigonal field and spin-orbit interaction and in the wave function characterization of the ground states.

One scheme proposed by J. Kanamori[10] considers the free Fe^{2+} ion symmetry as that of the rotation group $D^{(3)}$ which is initially split by the cubic portion of the crystalline field into a doublet E and a ground triplet T_2 with approximately 10,000 cm^{-1} energy separation (see Figure 4). In the remaining trigonal part of the crystalline field, the higher level persists as a doublet but the ground triplet is split approximately 100 cm^{-1} into an A_{1g} singlet and ground E_g doublet. The states are represented by $|L,M_L\rangle$ wavefunctions with the upper doublet as

$$\begin{aligned} |h1\rangle &= \sin\theta\ |2,2\rangle - \cos\theta\ |2,-1\rangle \\ |h2\rangle &= \sin\theta\ |2,2\rangle - \cos\theta\ |2,1\rangle \quad , \end{aligned} \tag{37}$$

the singlet as

$$|s\rangle = |2,0\rangle \tag{38}$$

and the ground doublet as

$$\begin{aligned} |g1\rangle &= \cos\theta\ |2,2\rangle + \sin\theta\ |2,-1\rangle \\ |g2\rangle &= \cos\theta\ |2,-2\rangle - \sin\theta\ |2,1\rangle \end{aligned} \tag{39}$$

where the angle θ depends on the ratio of the magnitudes of the cubic and trigonal fields (if the trigonal field is neglected, $\theta = \tan^{-1}\frac{1}{\sqrt{2}}$). In the ground state, L^z is diagonal with

$$L = \langle g1|L^z|g1\rangle = -\langle g2|L^z|g2\rangle = \frac{1+3\cos(2\theta)}{2} \tag{40}$$

while the matrix elements of L^x and L^y are zero. Using the estimate $\cos\theta = 0.838$ determined from the ratios of the quadrupole splittings of $FeCO_3$ and $FeSiF_6 \cdot 6H_2O$[12], a value of $\langle L^z \rangle = 1.1$ is obtained, while

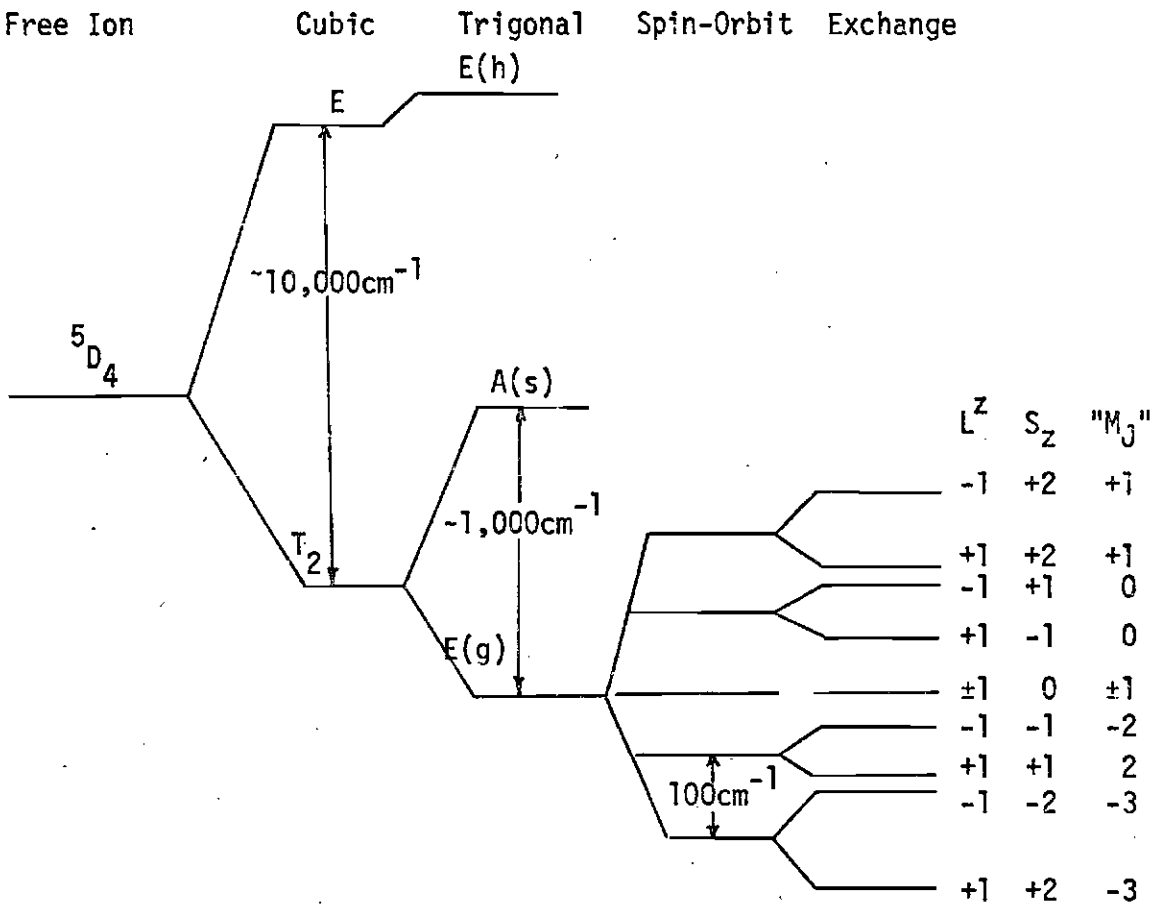

Figure 4. Fe^{2+} Splitting in $FeCO_3$ (after Kanamori[10]).

for $\theta = \tan^{-1}\frac{1}{\sqrt{2}}$, $\langle L^z \rangle = 1$. Introducing the Pauli spin matrix σ_z which operates on the two dimensional space spanned by $|g1\rangle$ and $|g2\rangle$, the first order spin-orbit coupling energy in the ground doublet is

$$\lambda \langle L \rangle \quad \sigma_z S_z. \tag{41}$$

Hence the ground doublet is further split into five doublets specified by

$$\sigma_z = 1,\ S_z = m \quad \text{and} \quad \sigma_z = 1,\ \ S_z = -m \quad (m = 2,\ldots,-2) \tag{42}$$

having a constant spacing $\lambda \langle L \rangle$ with the lowest doublet corresponding to $\sigma_z = 1$, $S_z = 2$ and $\sigma_z = -1$, $S_z = -2$.

Further splitting of the spin-orbit doublets may be due to an external magnetic field or an internal exchange interaction. The Zeeman energy is given by

$$\mu_B(2S_z + \langle L \rangle \sigma_z)H_z + 2\mu_B(H_x S_x + H_y S_y)\,. \tag{43}$$

where H is an external field. Since S_x and S_y have no matrix elements in the lowest spin-orbit doublet, only the first term remains, giving a splitting of 10 μ_B. With a field parallel to the c-axis, the second Zeeman terms could again be omitted, giving splittings of 10 μ_B, $6\mu_B$, $2\mu_B$ $2\mu_B$ and $6\mu_B$ for all the states with effective M_J values ($M_J = \langle L^z \rangle + S^z$) of ± 3, ± 2, ± 1, 0, and ∓ 1 respectively. Exchange interaction will also split the spin-orbit doublets expressed by the Heisenberg Hamiltonian as

$$H = -\sum_{ij} J(\overline{r}_i - \overline{r}_j)\overline{S}_i \cdot \overline{S}_j \tag{44}$$

where i and j refer to lattice sites and J is positive for ferromagnetic coupling and negative for the antiferromagnetic case. To consider anisotropic exchange equation (30) may be rewritten as

$$H = - \sum_{i,j} [J_{||}(\bar{r}_i - \bar{r}_j) S_i^z S_j^z + J_{\perp}(\bar{r}_i - \bar{r}_j) S_i^x S_j^x + S_i^y S_j^y] \qquad (45)$$

In the extreme anisotropic case, corresponding to an Ising system $J_{\perp} = 0$, and the Hamiltonian can be written as

$$H = - \sum_{ij} J_{ij} S_i^z S_j^z \qquad (46)$$

This same expression could also be assumed directly for the ground spin-orbit doublet in $FeCO_3$ since S^x and S^y have zero matrix elements. Assuming $J_{ij} = J$ to be constant for all spin-orbit levels, splittings of 4J, 2J, 0, 2J, and 4J for levels corresponding again to M_J values of ±3, I2, ±1, 0, and ∓1, respectively.

In the second scheme proposed by J. Griffith,[11] the free Fe^{2+} ion is split also by a cubic field into and upper doublet E and a ground triplet $^5T_2$. The d wave functions for the ground state are expressed in terms of L, M_L states as follows:

$$\begin{aligned} \varepsilon &, \ |dt_2 1\rangle = |2,-1\rangle \\ \eta &, \ |dt_2 0\rangle = \frac{1}{\sqrt{2}} (|22\rangle - |2\text{-}2\rangle) \\ \zeta &, \ |dt_2 \text{-}1\rangle = - |21\rangle \end{aligned} \qquad (47)$$

However, the p wave functions ($|1,1\rangle$, $|1,0\rangle$ and $|1,-1\rangle$) of the ^5P

representation transform under the operations of the cubic group, O, as the t wave functions. Hence a structural isomorphism exists between $^5T_2$ and ^5P. The t wave functions can be expressed in terms of the p wave functions which are in turn combinations of M_S,M_L states with $M_S = \pm 2, \pm 1, 0$ and $M_L = \pm 1, 0$:

$$\begin{aligned} &\varepsilon \ , \ |p1\rangle \\ &\eta \ , \ |p0\rangle \\ &\zeta \ , \ |p\text{-}1\rangle \ . \end{aligned} \tag{48}$$

By comparing matrix elements of L for ε, η and ζ in the t_2 and p representations, it is observed that the matrix of L within the t_2 representations of the d functions is equal to the matrix of -L for the p functions, i.e.

$$\langle p_i|L_k|P_j\rangle = -\langle dt_2 i|L_k|dt_2 j\rangle. \tag{49}$$

Consequently, for the Hamiltonian describing the remaining interactions, the sign of L is changed to give

$$H = \frac{1}{4}\rho\bar{L}\cdot\bar{S} + \delta(L_z^2 - \frac{2}{3}) + \beta\bar{H}\cdot(-\bar{L}+2\bar{S}) \tag{50}$$

where $(L_z^2 - \frac{2}{3})$ represents the trigonal distortion.

The effect of applying the first two terms of (50) to the correlated ^5P state is given in Figure 5. By plotting E/ρ as a function of $\omega = \delta/\rho$, the spin-orbit splitting is exhibited by the three levels at $\omega = 0$, and the effect of the trigonal distortion is indicated at finite ω values.

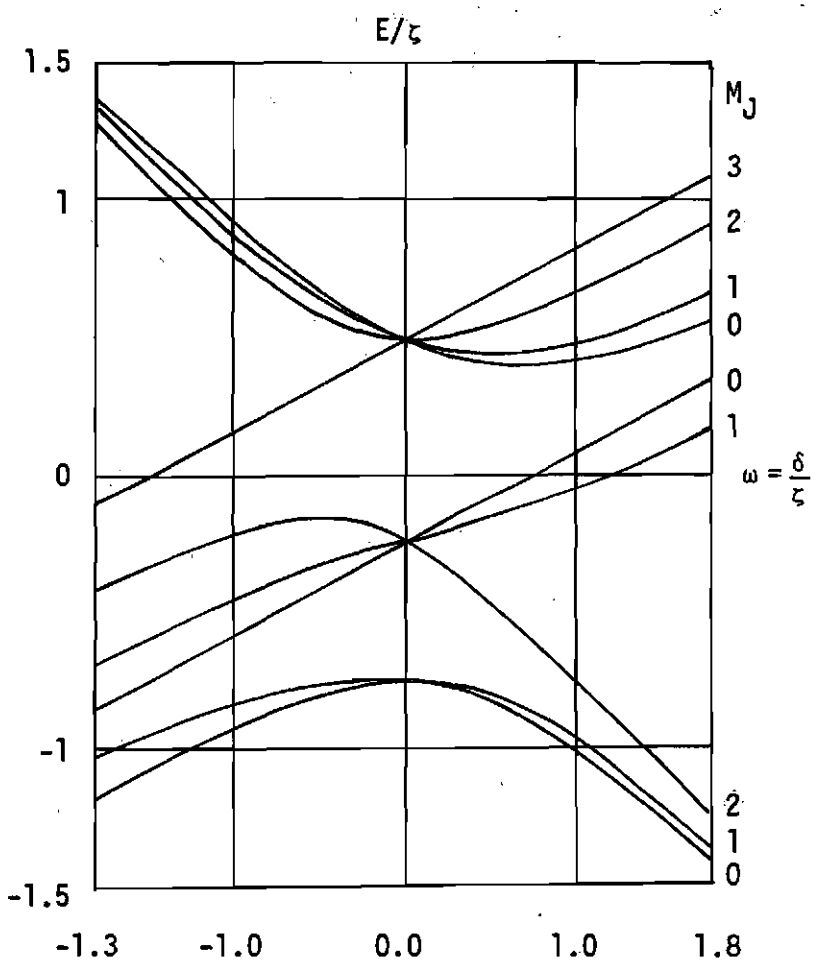

Figure 5. Splitting of the Ground Cubic Field Triplet of Fe^{2+} by Spin-Orbit Coupling and the Trigonal Field. (from Griffith[26])

CHAPTER III

THE EXPERIMENTS

The Samples

Impurity analyses were performed on all the samples used and geographical location was known for most of the natural crystals.

The experimental observations of siderite were independent of geographical source and optical appearance. The samples studied came from Quebec, Greenland and Connecticut. Raman excitations of the same energy were found in all samples. Also, while there was a color variation from clear light brown to opaque dark brown between samples or within a single sample, spectrochemical analysis revealed essentially the same impurity concentrations in both optical extremes. Further electron microprobe analyses revealed a 4% Mn concentration by atomic weight while Mg (2%), Si (0.5%), Ca (0.5%) and Al (0.2%) were the remaining significant contributions. The 4% Mn concentration was verified by neutron activation analysis on both clear and opaque samples. The detailed impurity analysis results for siderite and the other samples studied are given in Appendix A.

The remaining natural carbonate crystals studied were rhodochrosite ($MnCO_3$), dolomite ($CaMg(CO_3)_2$), and calcite ($CaCO_3$). In the rhodochrosite from Colorado, electron microprobe analysis revealed mainly Co (0.09%) and Ca (0.07%). A large 6% Fe concentration with Si (0.4%) and Mn (0.6%) were found in addition to the expected Ca and Mg in the dolomite from

Brazil. No analysis was considered necessary on calcite based on its colorless transparency and expected Raman spectra.

The remaining work was performed on synthetic $FeCO_3$ powder grown for Dr. H. Mook at the Oak Ridge National Laboratory. Microscope photographs indicate the particle size to be on the order of 1 micron and microprobe results reveal Si (.02%), Mn (.007%) and Na (.001%).

The Raman Scattering Apparatus

The exciting source at the inception of the experimental work was an argon ion laser (Coherent Radiation Model 52) with an output of 1300 mw of light at 5145 Å polarized vertically with respect to the laboratory. Later the laser was modified by the addition of a beryllium oxide plasma tube and a light intensity stabilization loop; the new power at 5145 Å was 1.5 W. The standard Raman scattering arrangement is given in Figure 6. The initially horizontal laser light was first focused and then rotated 90^{o} by a mirror so that the scattering column was parallel to the vertical slits of the spectrometer. The scattered light was then focused into the slits of a Spex (Model 1401) 3/4 meter Czerny-Turner double monochromator spectrometer. When scans of particular polarization tensor components were required, a polaroid sheet on a rotatable mount was placed between the lens and spectrometer to select polarizations parallel or perpendicular with respect to the incident beam polarization followed by a scrambler to prevent enhancement of particular components by the spectrometer. Typical slit widths were 50, 100, and 50 microns, and the entrance slit height was 10 mm. The gratings had 1200 grooves/mm and were blazed at 5000 Å. On most of the spectra taken, the scan speed

was either 50 or 100 cm^{-1}/min.

The photomultiplier tube was on ITT Startracker (Model FW 130) with an effective photocathode surface of rectangular shape (10 mm x 2 mm). The surface had an extended red sensitivity (S - 20). The room temperature dark count rate of 120 cts/sec. was reduced to 3 cts/sec. by cooling the tube to -20°C with a thermoelectric refrigerated chamber (Products for Research Model TE-104). The photocathode was operated at -1500 volts by a Tennelec power supply (Model AEC-100).

The photomultiplier was followed by a preamplifier-amplifier-discriminator unit (Nuclear Data Model 520). The uniform output pulses of the discriminator were counted by a rate meter (Tennelec Model TC 590) and the signal was recorded on a strip-chart recorder (Honeywell Electronik 194). Typical recorder speeds were 1 or 2 min/in. which when combined with the scan speeds gave spectra displays of 50 to 100 cm^{-1}/in.

Low Temperature Apparatus

Low temperatures were obtained with either a helium gas refrigerator (Cyrogenic Technology Inc. Model 350) or a liquid helium dewar (Janis Super Vari-Temp Model W-DT).

The lowest temperature obtainable with the helium refrigerator was 12°K at the top of the second stage. However, after the sample was securely mechanically mounted for optical measurements at the bottom of the second stage, the lowest temperature obtained at the sample was 22°K.

Temperatures down to 6°K were obtained with the liquid helium dewar. Although the dewar is capable of obtaining temperatures up to room temperature, it was used mainly for taking data from 6°K to 100°K,

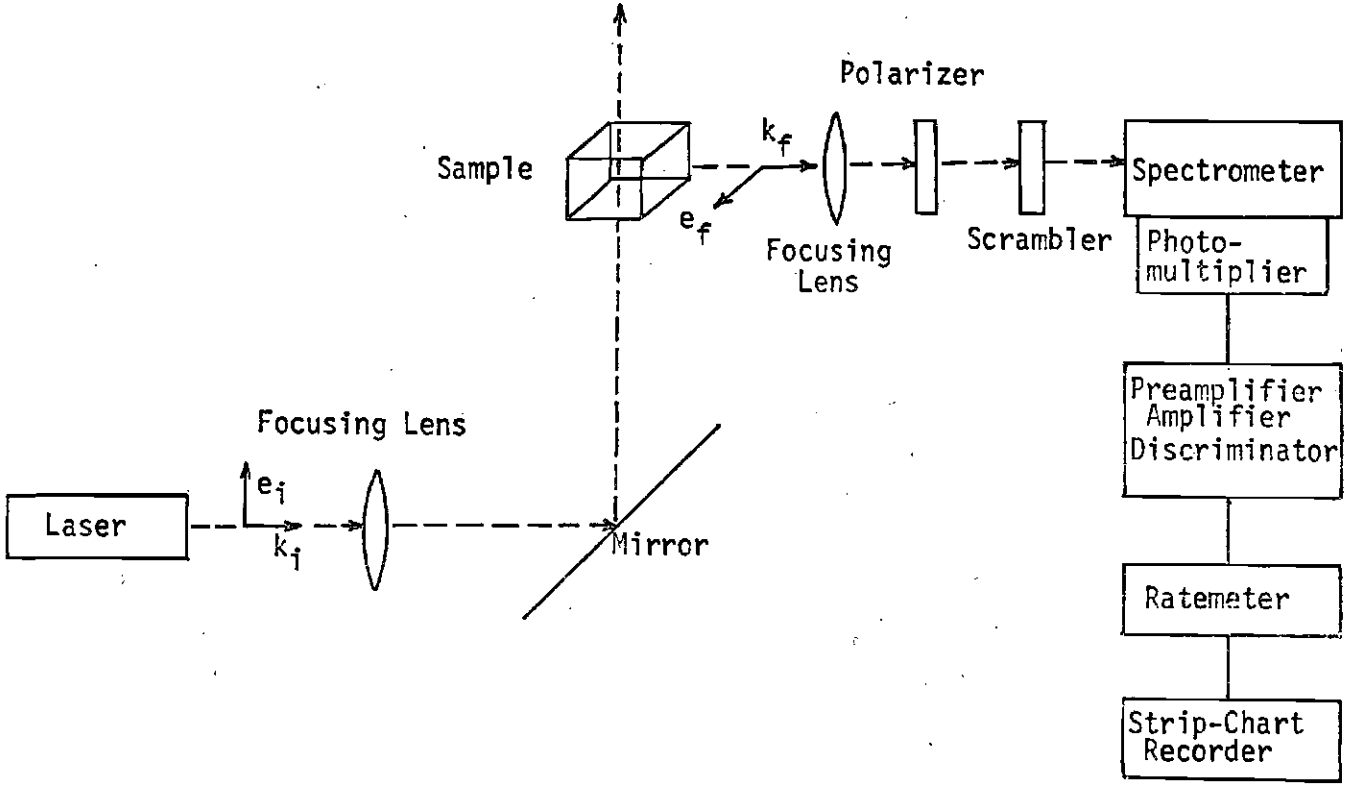

Figure 6. The Standard Raman Scattering Equipment Arrangement.

with the helium refrigerator used for the higher temperatures. The tail section of the dewar was modified by the addition of a third window (at the level of the existing two windows) to make collection of light scattered 90^{o} possible.

Sample temperatures in both the dewar and refrigerator were measured with platinum resistance thermometers. The thermometers had room temperature resistances of either 500 ohms (Rosemount Model 146 MA or 118 AEM) or 100 ohms (Rosemount Model 118 GX). The thermometers were mounted directly on the crystal sample surfaces with a thin piece of indium between the thermometer and sample for increased thermal conductivity. Thermometer voltages were measured by standard techniques using a Leeds Northrup Model potentiometer.

CHAPTER IV

RESULTS AND DISCUSSION

Presentation of the Data

The Raman data is presented in plots of intensity of scattered light versus frequency shift of the scattered light from the incident laser frequency. The frequency will be indicated in units of reciprocal centimeters, cm^{-1} ($3\ cm^{-1} = 100\ GH_z$). The scattering geometry for oriented crystals is indicated by placing the polarization tensor component measured inside parenthesis and the direction of the incident and scattered light (with respect to the crystal axes) before and after the parenthesis, respectively. For example, a spectrum of the α_{yz} components obtained with initial and final beam directions of z and x, respectively, would be indicated as z(yz)x.

Siderite Raman Data at Liquid Helium Temperature

Since calcite, natural $CaCO_3$, and siderite both belong to the same space group, D_{3d}^6, essentially the same vibrational Raman spectra should be observed in both samples at the same temperature. The same lines corresponding to the same symmetry species and atomic motion should occur in both spectra. The basic difference is a shift in energy between lines corresponding to the same atomic motion due to the different atomic masses and force constants. Among the carbonate crystals, this difference is usually less than 30 cm^{-1}.

First the Raman spectrum of calcite at room temperature (297°K) is presented in Figure 7. Only the expected Raman active vibrational lines are observed. The symmetry species ($A_{1g} + 4E_g$) are indicated on the corresponding peaks along with a frequency enumeration (ν_1 and $\nu_{10} - \nu_{13}$). The atomic motions corresponding to these enumerated Raman frequencies along with the atomic motion for all the modes of D^6_{3d} symmetry is given in Figure 8. The designation of these atomic motions is based on results of Raman and infrared spectra and eigenvalue calculations on calcium carbonate and on lithium, sodium, and potassium nitrate.[22]

The complete Raman spectrum of siderite at 6°K is presented in Figure 9. A high sensitivity scan at 6°K from 800 cm^{-1} to 1900 cm^{-1} is given in Figure 10. As in the case of calcite, the expected vibrational modes are identified. There are also six additional lines indicated by their frequencies at 6°K: 440, 741, 820, 1175, 1225, 1485, and 1735 cm^{-1}. The intensity of all these lines decreases with increasing temperature with only three observable at room temperature. The additional lines can be categorized as these with temperature dependent frequencies (440, 1175, and 1225 cm^{-1}) and those with frequencies which do not vary with temperature (741, 870, 1495 and 1735).

Siderite Raman Lines with Temperature Dependent Frequencies

Lines having temperature dependent frequencies were studied by taking scans only over frequency regions containing each particular excitation. The scans were taken at different temperatures starting from 6°K and proceeding to at least 60°K in all cases. The temperature was

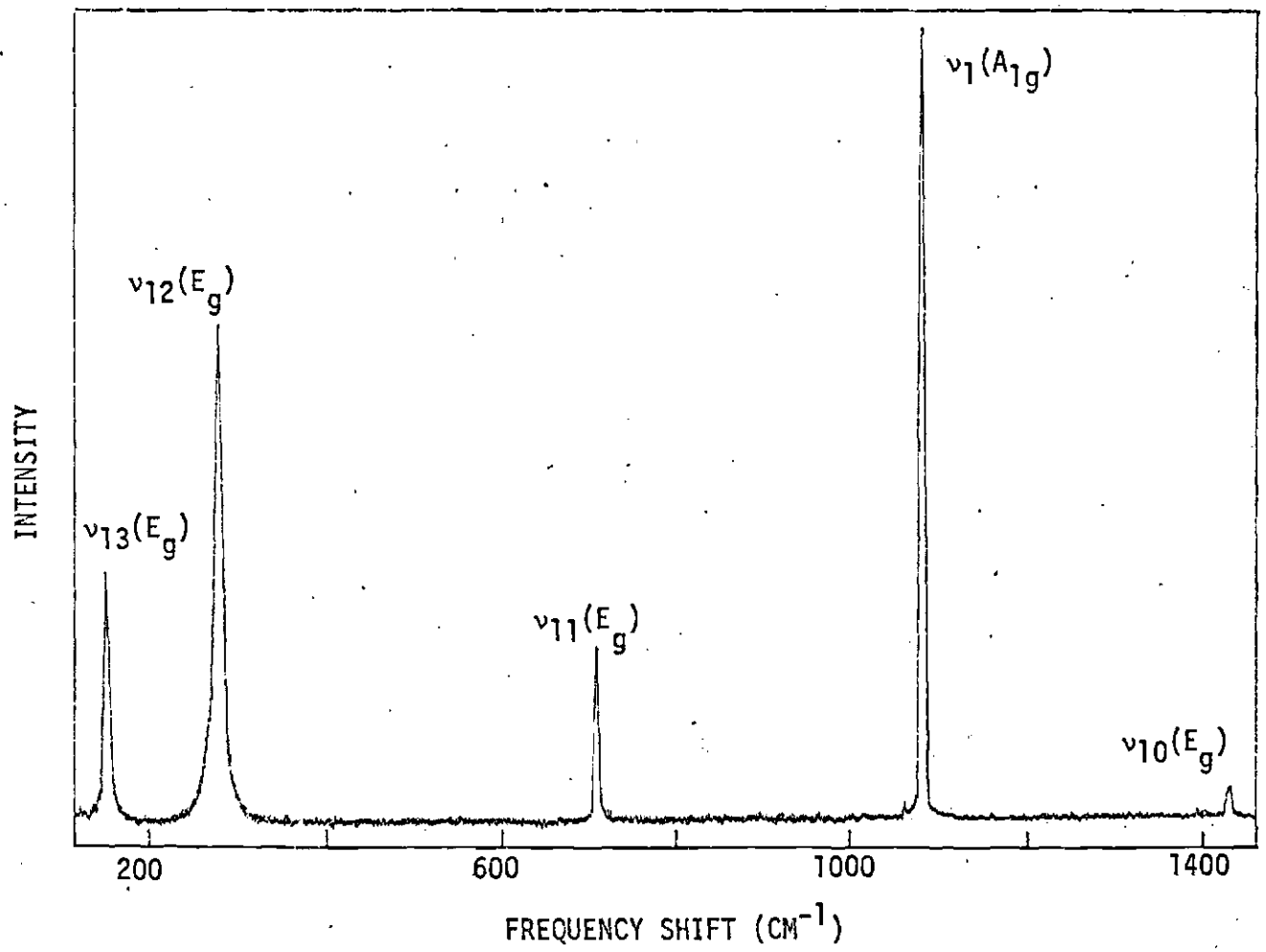

Figure 7. Raman Spectrum of Calcite at 297°K.

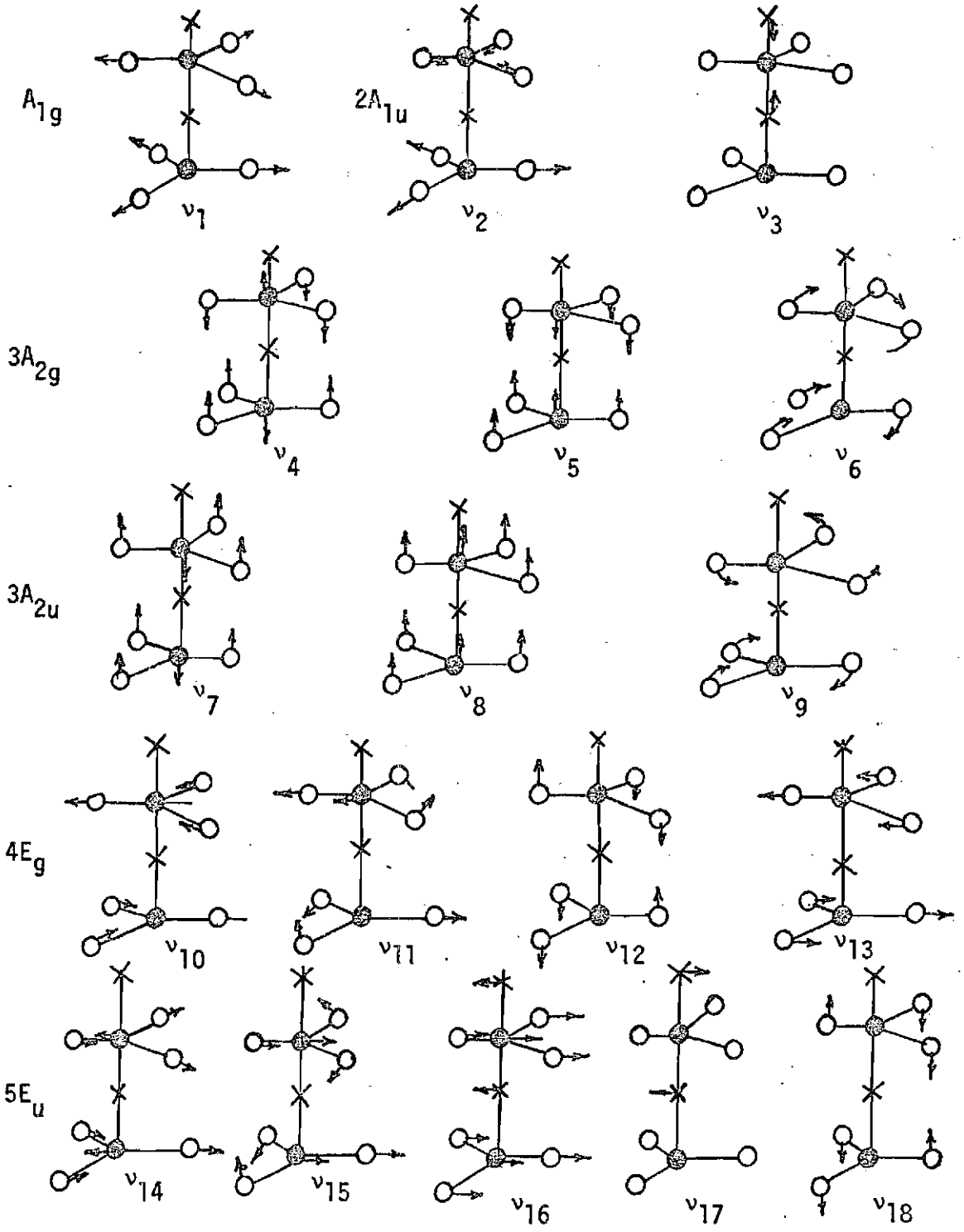

Figure 8. The Atomic Motion of Symmetry Species of the D^6_{3d} Crystals.[22]

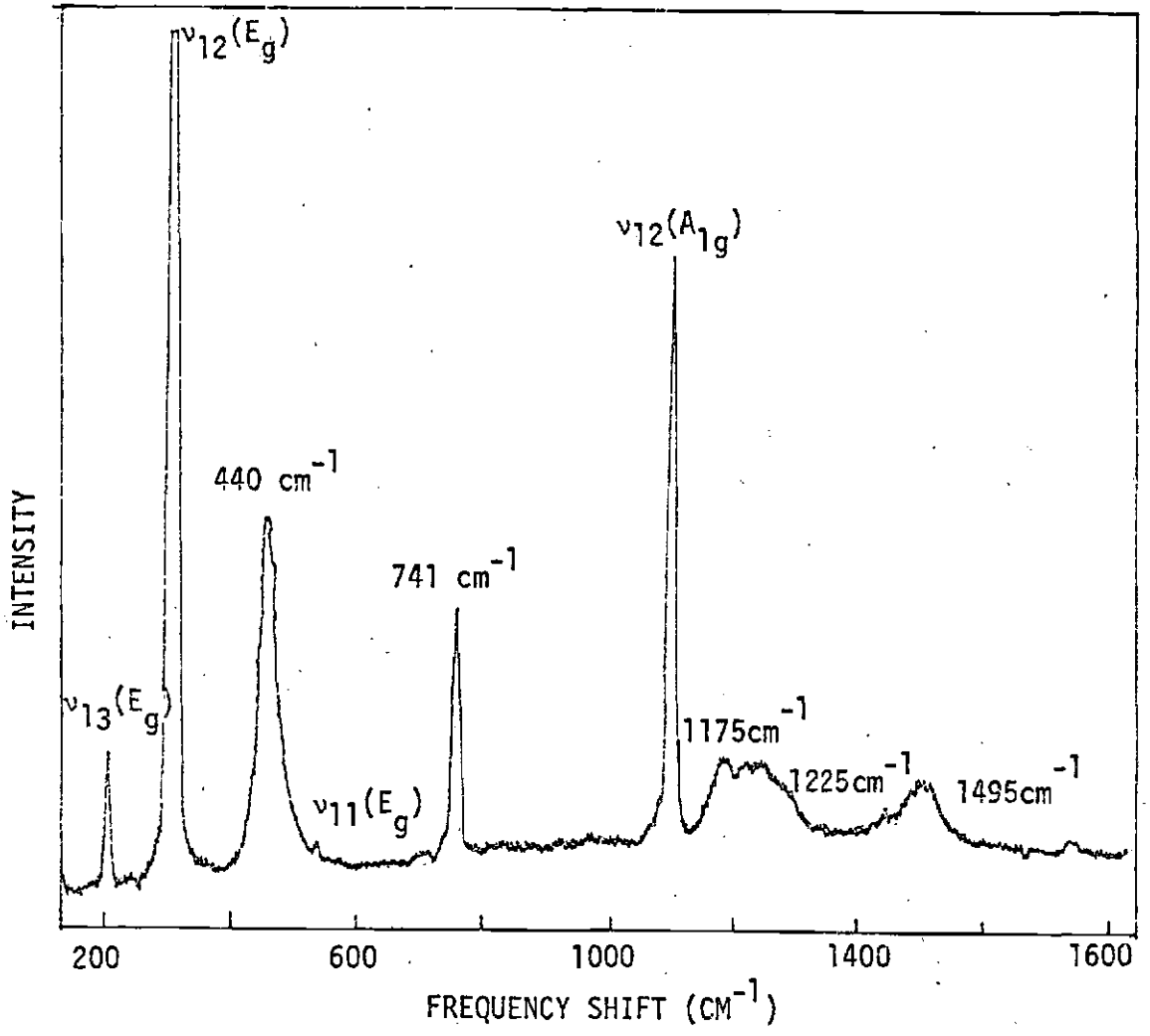

Figure 9. Raman Spectrum of Siderite at 6°K.

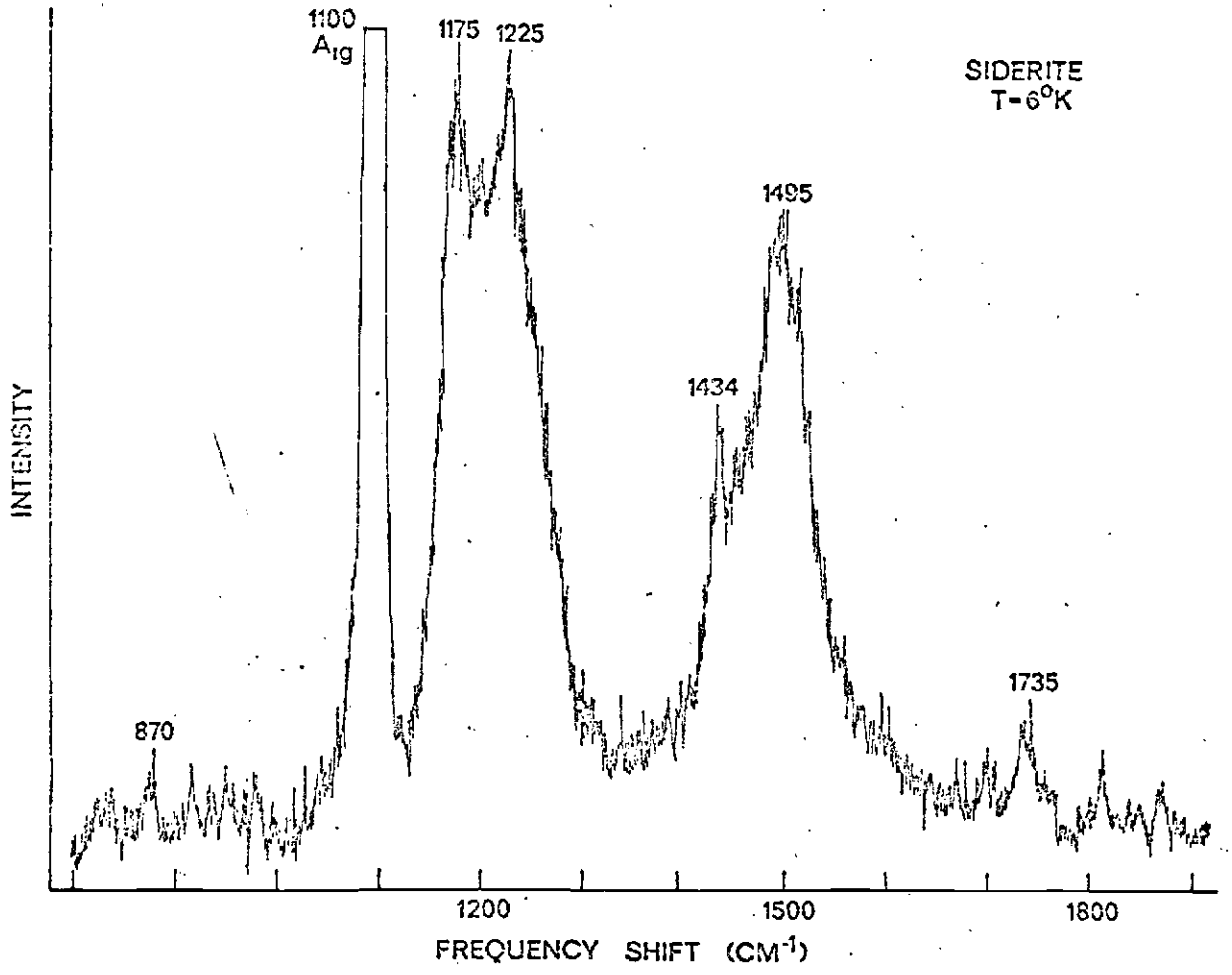

Figure 10. Raman Spectrum of Siderite at 6°K (800 cm^{-1} to 1900 cm^{-1}).

stabilized to within ± 1°K during each scan. In addition to the change in frequency of the peaks, there was a broadening of the lines accompanied by a decrease in intensity as the temperature is increased.

Plots of frequency versus temperature in Figure 11 reveal that the most rapid frequency shift occurs near the Néel temperature (38°K). The 440 cm^{-1} line increases in frequency more sharply in the region from 20°K (440 cm^{-1}) to 38°K (460 cm^{-1}) than in the region from 38°K to room temperature (525 cm^{-1}). Similarly, the 1225 cm^{-1} line has its greatest change below the Néel temperature (from 1180 cm^{-1} at 38°K to 1200 cm^{-1} at 48°K). In addition, it returns to its lower frequency at about 58°K. The complete temperature variation of the 440 cm^{-1} line from 6°K to room temperature is given in Figure 12 where the frequency variation above the Néel temperature is found to be generally linear.

In Figure 13, the integrated intensity of the 440 cm^{-1} line is presented. The integrated intensity of the 440 cm^{-1} line increases as the temperature is decreased from room temperature to 70°K. However, there is a variation from the consistent increase as the temperature is further lowered through the critical temperature to 6°K as shown in Figure 13. There are two distinctive features. One is the relatively rapid increase from 41°K with a peak at 38°K followed by a rapid decrease to a minimum around 28°K. The other is the increase as the temperature is lowered below 28°K with integrated intensity values below 17°K being higher than that at 38°K.

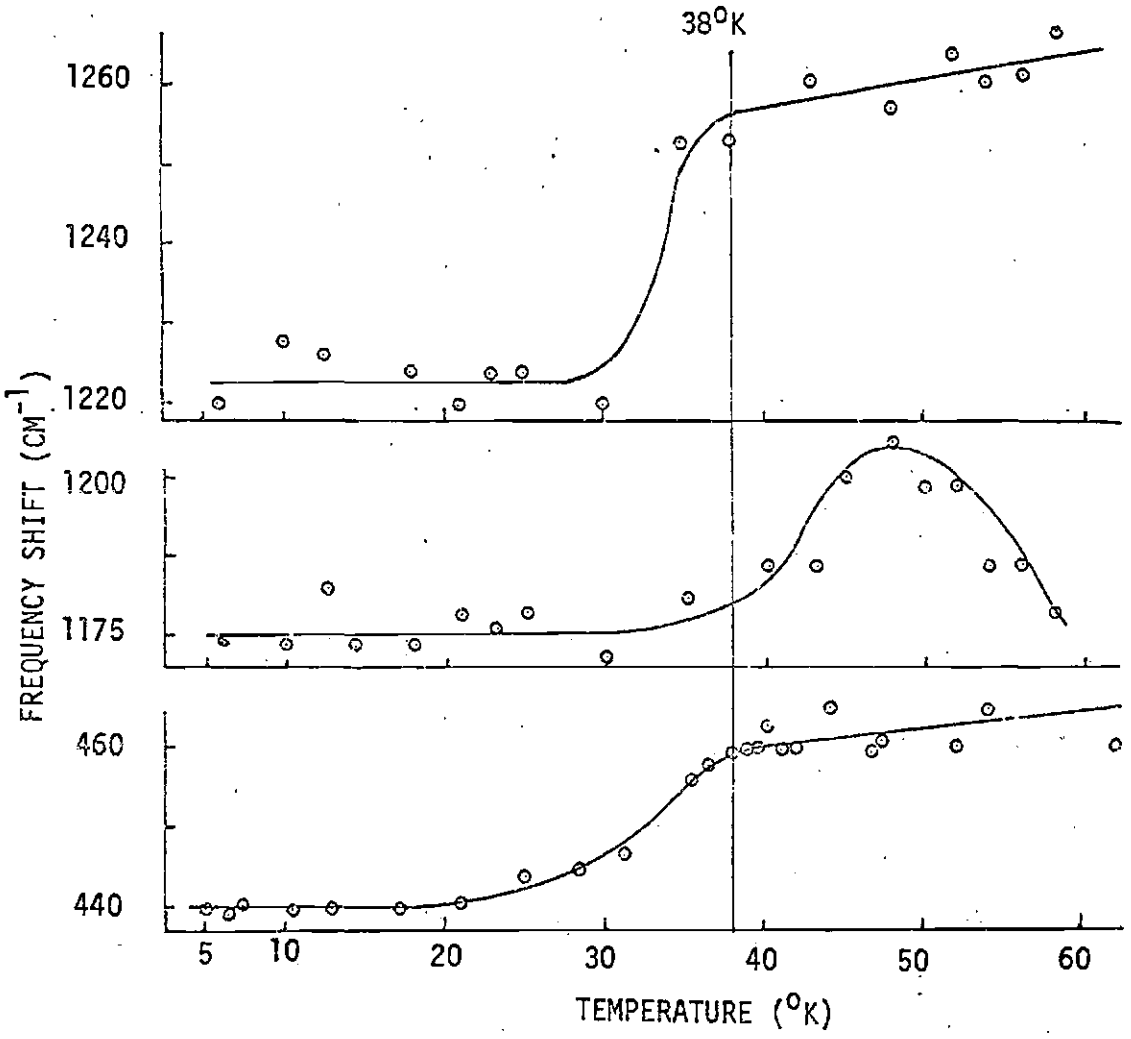

Figure 11. Temperature Dependent Raman Lines in Siderite. Frequency versus Temperature.

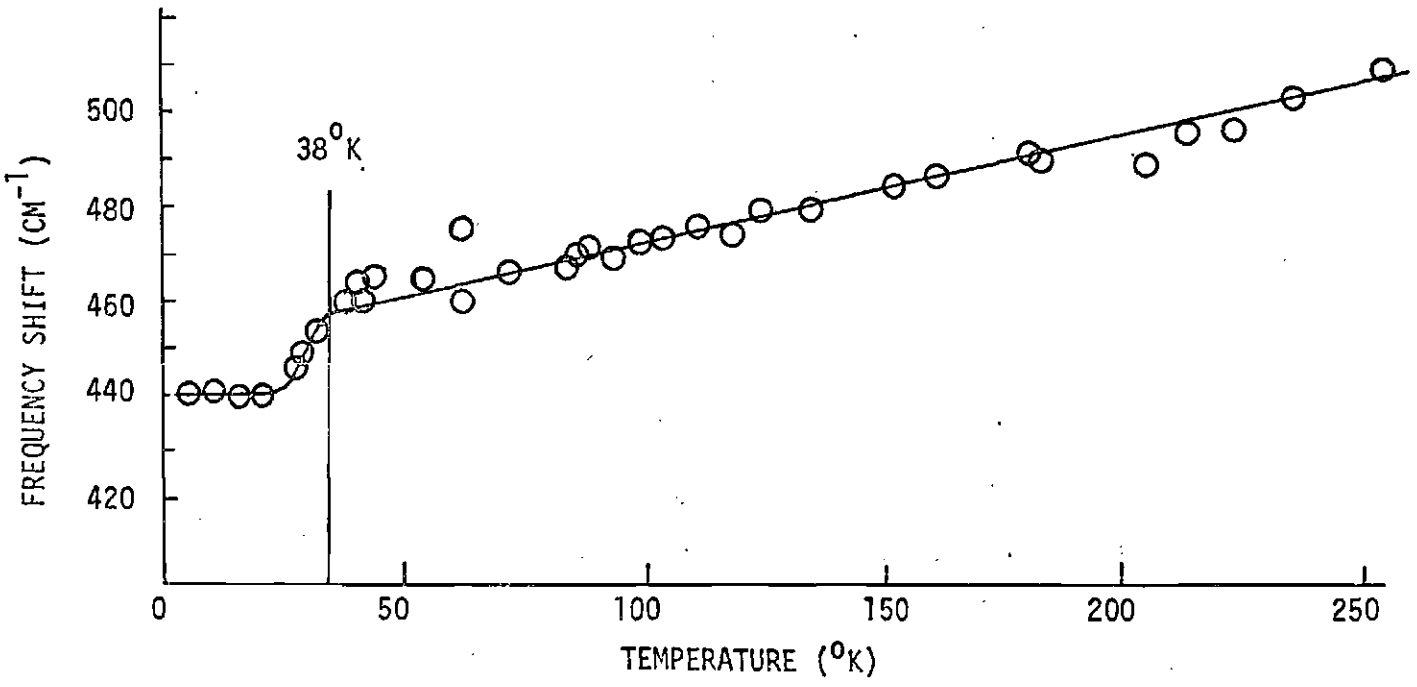

Figure 12. Frequency Variation with Temperature of 440 cm^{-1} Siderite Raman Excitation.

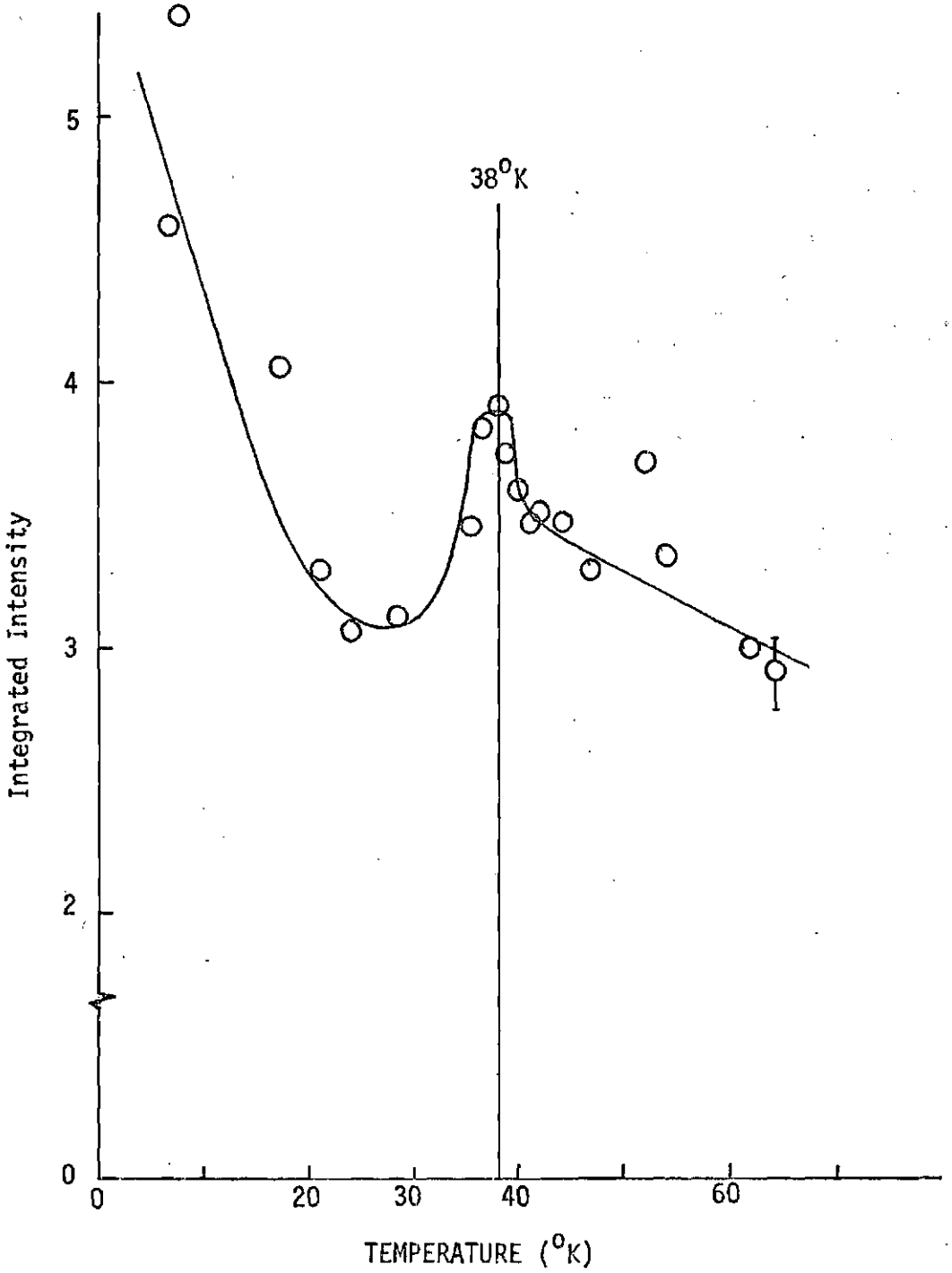

Figure 13. Integrated Intensity of Siderite 440 cm^{-1} Line as a Function of Temperature.

Siderite Raman Excitations with Temperature Independent Frequencies

Of the lines with temperature independent frequencies, the behavior of the 741 cm^{-1} line is the most interesting. As shown in Figure 14, the 741 cm^{-1} line begins as an asymmetry in the 731 cm^{-1} E_g line (ν_{11}) at room temperature. As the temperature is lowered, this asymmetry reveals itself as a new line at 741 cm^{-1}. The 741 cm^{-1} line continues to grow in intensity compared to the 731 cm^{-1} line as the temperature is lowered until at 6^oK, the 731 cm^{-1} exists only as an asymmetry in the 741 cm^{-1} line.

The variation of the integrated intensity of the 741 cm^{-1} line with respect to temperature is presented in Figure 15. To isolate the 741 cm^{-1} variation from the 731 cm^{-1} E_g (ν_{11}) line, areas were measured on the higher frequency side with the frequency at the maximum intensity taken as the lower limit. The integrated intensity of the 741 cm^{-1} line generally increases as the temperature is decreased from temperature to 6^oK. However, below 28^oK the integrated intensity does not continue to increase but remains approximately constant. Also, the points appear to indicate a relative maximum at 38^oK (T_N) followed by a relative minimum at 34^oK, but this is not certain considering the error estimates of the points.

Raman Polarization Tensor Components of Siderite

Scans of five of the Raman polarization tensor components were taken. Scans of α_{xx}, α_{yy}, and α_{zz} for which both E_g and A_{1g} modes should appear and scans of α_{yx} and α_{yz} which favor the E_g modes were taken at 6^oK. The optical quality of the particular crystal used in these scans

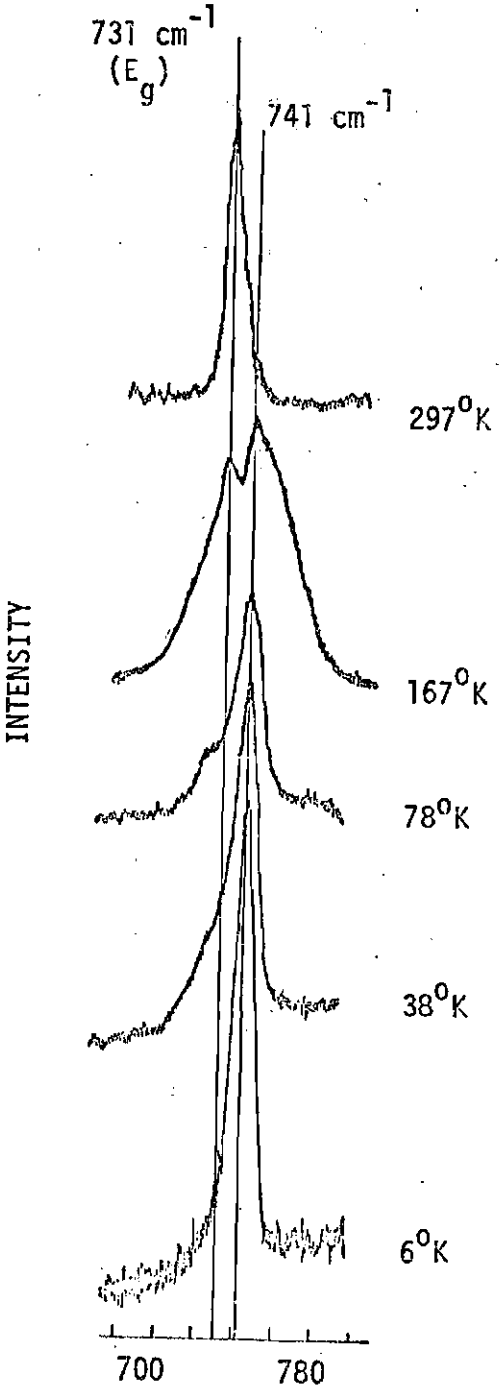

Figure 14. Raman Spectra of 731 cm^{-1} and 741 cm^{-1} Excitations in Siderite at Temperatures from 6°K to 297°K.

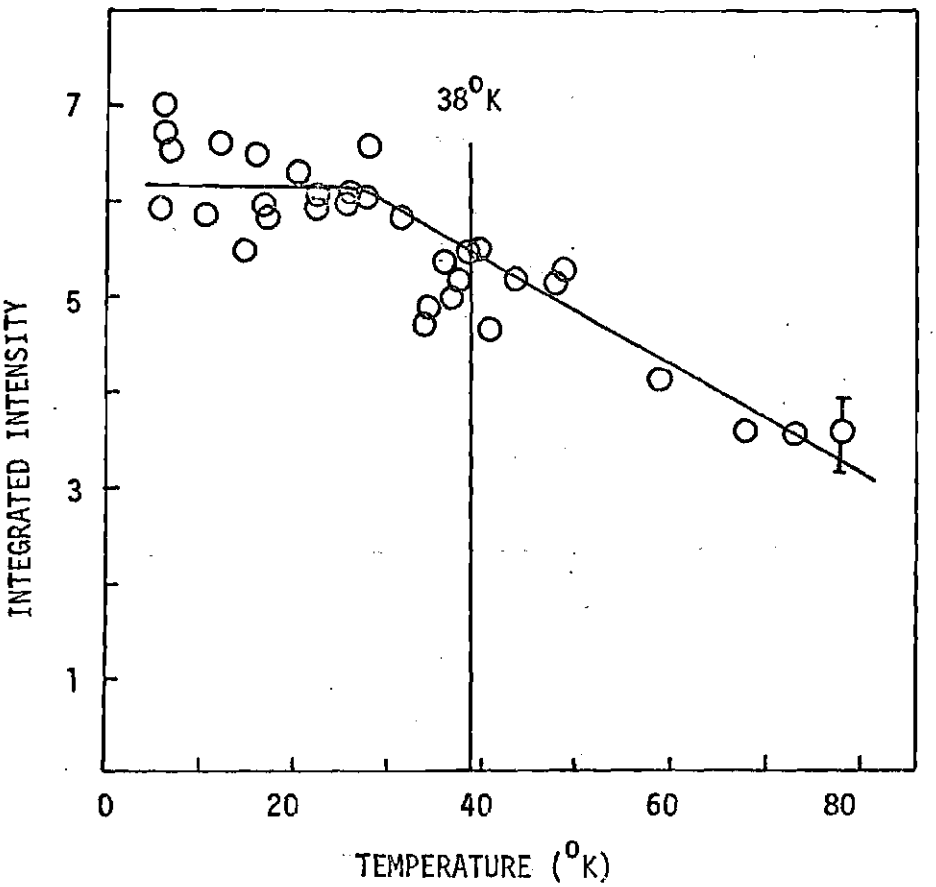

Figure 15. Integrated Intensity of Siderite 741 cm^{-1} Excitation versus Temperature.

and the fluorescence background permitted only the 440 cm^{-1} and the 741 cm^{-1} lines to be observed.

It was observed from the scans that the vibrational lines do not follow the predicted polarization selection rules. For example, there should not be an A_{1g} peak in the α_{yx} or α_{yz} scans or E_g peaks in α_{zz}. These discrepancies may be due to depolarization of the incident beam while traversing the crystal. Optical imperfections and impurities in the crystal cause the initial beam direction to be deviated and the initial polarization vector to be rotated. The same problems may occur with the beam emerging from the crystal.

However, some knowledge of the behavior of the 440 cm^{-1} and 741 cm^{-1} lines can be obtained by comparing their intensities with the experimentally observed intensities of the E_g and A_{1g} vibrational modes. By comparing the intensities of the lines in the z(xx)x scan with the intensities in the remainder of the scans, it appears that both the 440 cm^{-1} and 741 cm^{-1} lines follow the intensity pattern of the averaged 187 cm^{-1} and 287 cm^{-1} E_g intensities rather than the A_{1g} line as shown in Table 2. The main exceptions are the x(zz)z and z(yz)x scans.

Raman Data of Synthetic $FeCO_3$ Powder

The Raman spectra of the synthetic $FeCO_3$ powder were quite different from the siderite spectra. Only the 1087 cm^{-1} powder line is close enough in frequency and intensity to the 1090 cm^{-1} siderite line to be designated as an identical A_{1g} mode. Some of the remaining dominant lines could be classified as E_g modes (153 or 161, 267, and 725 or 896 cm^{-1}) but the frequency differences between two forms (synthetic powder

Table 2. Ratio of Intensities in Polarized Scans to Intensities in z(xx)x Scan

Polarization		Frequencies (cm^{-1}) 187	287	440	741	1087	187,287 Intensities Avg.
	1. z(xx)x	1	1	1	1	1	1
	z(yy)x	.31	.124	.198	.368	.88	.217
	2. x(yy)z	.546	.286	.535	.58	.975	.416
	x(yy)z	.165	.055	.138			.110
	x(zz)z	.069	.79	.216	.526	.193	.430
	3. x(zz)z	.108	.580	.258	.368	.150	.349
	4. x(yx)z	.486	.336	.380	.526	.396	.411
	5. z(yz)x	.148	.815	.390	.685	.183	.482

and natural crystal) of the same compound cannot be justified.

Ferrous Carbonate Infrared Absorption Data

Infrared absorption spectra have also been taken of both siderite and the synthetic $FeCO_3$ powder. Although the spectrometer permitted spectra to be taken from near 200 cm^{-1} to 4000 cm^{-1}, analysis below 300 cm^{-1} is indefinite due to the infrared activity of the KBr pellet material (in which the iron carbonate samples were mixed) in that region.

Also, since the Raman work did not go above 2200 cm^{-1} and since the infrared spectra did not indicate any unusual activity there, the scans will be presented only to 2200 cm^{-1}.

In Figure 16, the infrared absorption spectra of siderite is presented. The most intense peaks are the expected infrared modes at 741 cm^{-1} (ν_{15}, E_u), 870 cm^{-1} (ν_7, A_{2u}) and 1412 cm^{-1} (ν_{14}, E_u). Where the frequency notation is the same as that for the modes in Figure 8. In addition, there appears an asymmetry in the 741 cm^{-1} line centered around 731 cm^{-1}, another asymmetry in the 1412 cm^{-1} line around 1470 cm^{-1}, and a separate line at 1802 cm^{-1}.

Similar expected infrared lines are also found in the spectra of the synthetic $FeCO_3$ powder at 747, 869, and 1425 cm^{-1}. There are also new lines not present in the siderite spectra. There are two separate lines at 815 and 1080 cm^{-1} and an asymmetry in the 869 cm^{-1} line at 840 cm^{-1}. However, absent are the asymmetries at 731 cm^{-1} and 1470 cm^{-1} observed in the siderite spectra.

A summary of the Raman and infrared excitations in siderite and synthetic $FeCO_3$ powder is presented in Table 3. In the case of the synthetic $FeCO_3$ powder Raman excitations, the strong lines are designated with an (S), and the remaining lines are very weak.

Raman and Infrared Studies on Similar Crystal Systems

Further Raman and infrared studies were performed on two similar crystal systems, dolomite (natural $CaMg(CO_3)_2$) and rhodochrosite (natural $MnCO_3$). They were of interest because in addition to belonging to the D^6_{3d} space group, lines other than the expected vibrational lines were

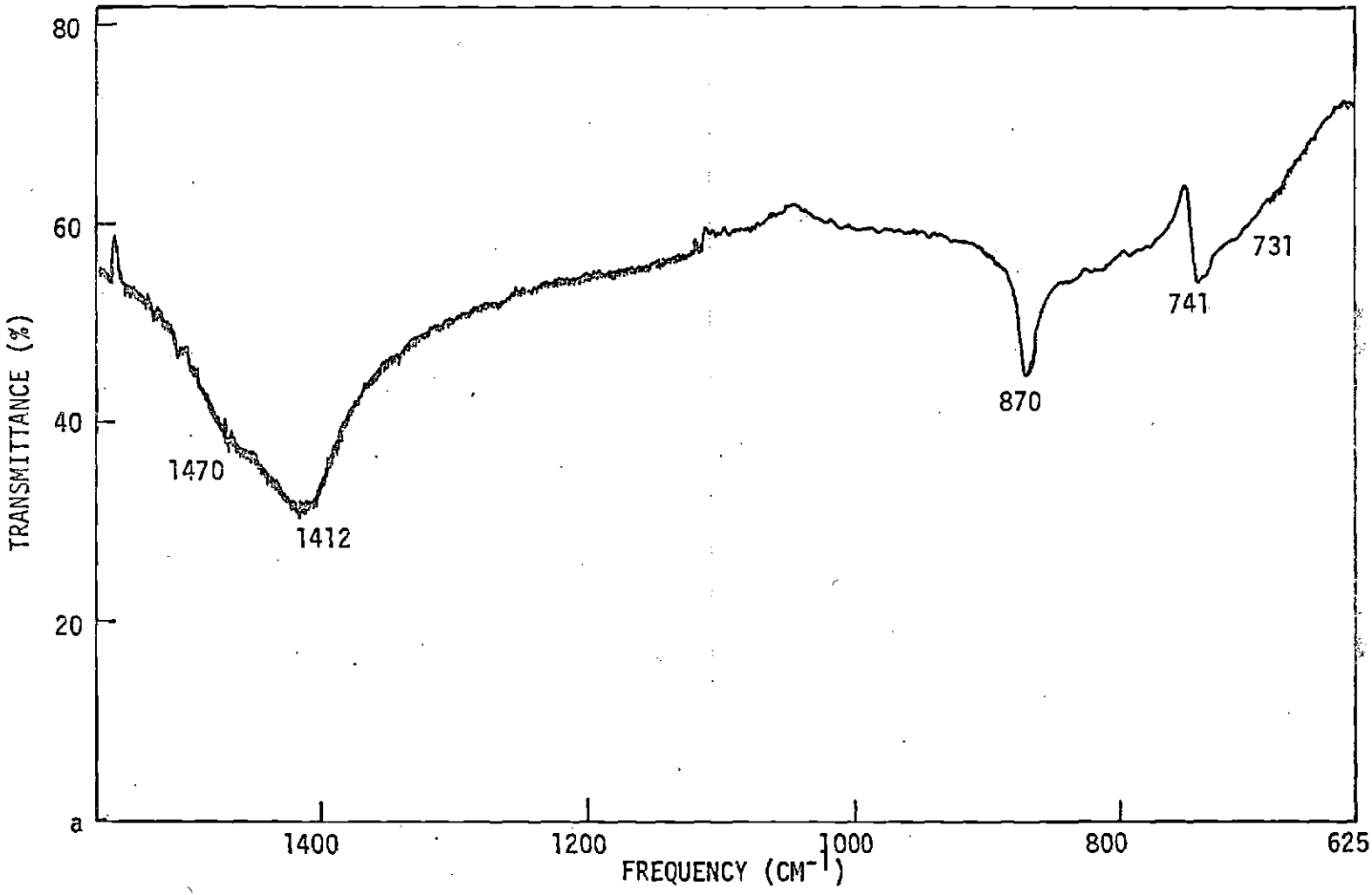

Figure 16. Infrared Absorption Spectra of Siderite (at Room Temperature).

Table 3. The Raman and Infrared Lines of Siderite and Synthetic $FeCO_3$ Powder

Siderite-$FeCO_3$			Synthetic $FeCO_3$ Powder	
Raman (expected vibrational)	Raman (unexpected)	Infrared	Raman	Infrared
187(ν_{13})-Eg			63,76(S),113(S)	
300(ν_{12})-Eg			153,161	
	440 to 515			
731(ν_{11})-Eg	741	741(ν_{15})E_u	210,267(S) 286,300,327,368	
	870	870(ν_7)A_{2u}		
1090(ν_1)A_{1g}	1175 to 1200		522,725	741(ν_{15})-E_u
	1225 to 1260		896(S),942	815,840
		1412(ν_{14})-E_u		870(ν_9)-A_{2u}
1434(ν_{10})Eg	1495	1475	1009,1087(S)(ν_1)Ag	1080
	1735		1197,1238,1300	
				1412(ν_{14})-E_u

observed in their Raman spectra.

The Raman and infrared lines are summarized in Table 4. The Raman and infrared data were obtained from the same samples. Based on frequency comparisons, none of the extra Raman lines can be identified as infrared modes that have become Raman-active. The main similarity to the extra siderite lines is the increasing intensity with decreasing temperature.

Table 4. The Raman and Infrared Lines in Dolomite and Rhodochrosite

Dolomite-$CaMg(CO_3)_2$			Rhodochrosite-$MnCO_3$		
Raman (expected vibrational)	Raman (unexpected)	Infrared	Raman (expected vibrational)	Raman (unexpected)	Infrared
177(ν_{13})-Eg			185(ν_{13})Eg		
297(ν_n)-Eg	293		290(ν_{12})Eg	460	
				491	
					728(ν_{15})-E_u
	504(S)				
741(ν_{11})-Eg	728	729(ν_{15})-E_u	721(ν_{11})Eg	890 to 909	866(ν_7)-A_{2u}
	940	880(ν_7)-A_{2u}		940	
1098(ν_1)-A_{1g}		1420(ν_{14})-E_u		1030	
			1087(ν_1)Ag	1199	
				1310	
1446(ν_{10})-Eg	1755(S)	1808		1390	1410(ν_{14})-E_u
				1434(S)	
				1590	
				1675	
			1416(ν_{10})Eg	1730(S)	1795
				1804	

Some extra lines are present at room temperature: 293, 728 and 940 in dolomite; 890, 940, 1030, 1450, 1194, 1310, 1390, 1590, 1730 and 1804 in rhodochrosite. The remainder became apparent as the temperature is lowered (to $6^{o}K$ in both cases). However, this intensity growth appears to be mainly a decrease in linewidth rather than an integrated intensity increase. Also, there is no frequency shift with decreasing temperature, except for the 890 cm^{-1} line which shifts to 909 cm^{-1} at $6^{o}K$ in rhodochrosite.

Impurity Analysis of the Samples

The samples studied in this research were analyzed for impurities by three different methods: electron microprobe, spectrochemical analysis, and neutron activation. The results presented in Table 5 are listed in two rows. The upper row is the impurity percentage with respect to the total weight of the sample as reported by the analyst. The lower row is calculated from the upper row values to give the impurity percentage with respect to the number of cations.

For the electron microprobe a typical spot diameter was 200 micrometers with a probable penetration of 2 or 3 micrometers.

Discussion of Research by Other Groups Involving Siderite Raman Excitations

During this series of experiments, two papers were published which involved some of the extra siderite Raman excitations.[12,27]

One of the papers (Popkov et al.) involved temperature dependent Raman studies on siderite with results similar to those given here. However, there are some differences in the experimental results and conclusions.

Table 5. Summary of Impurity Analyses

Sample	Impurity								Method
	Si	Mn	Ca	Mg	Al	Fe	Na	Co	
Siderite	.01 .04	.01 .02	.005 .015						Electron microprobe
Siderite	.5 2	3 6	.5 1.5	2 8	.2 .8	81.7			Electron microprobe*
Siderite (clear)	.04 .16	.05 .1							Spectrochemical
Siderite(opaque)	.02 .08	.05 .1	.002 .006						Spectrochemical
Siderite (clear)		4 8							Neutron activation
Siderite(opaque)		3.8 7.6							Neutron activation
Dolomite	.42 .8	.63 .6	21 50	7.5 42.9	.05 .1	6 6			Electron microprobe
Rhodochrosite		99.52	.07 .21	.01 .04	.008 .032		.005 .02	.09 .18	Electron microprobe
$FeCO_3$ Powder	.02 .08	.007 .014				99.9	.001 .004		Electron microprobe

For each sample entry, the upper row designates the impurity percentage by weight and the lower row designates percentage of number of cations.

*This analysis was performed by the Oak Ridge National Laboratory. All other analyses were performed by the Georgia Tech Engineering Experiment Station.

The highest frequency E_g line (ν_{10} at 1434 cm^{-1}) along with the unexpected 870, 1175, 1225, and 1495 cm^{-1} lines were not found by Popkov et al. Also, the 748 cm^{-1} excitation at 4.2°K is classified as the $E_g(\nu_{11})$ mode, while as reported previously in Section IV.3, the strong excitation of 731 cm^{-1} line at room temperature is considered the E_g mode and the 748 cm^{-1} line which grows in intensity as the temperature is decreased is considered an additional excitation. There is also question about the designation of certain additional excitations to energy levels following the Kanamori scheme. The classification of the 1743 cm^{-1} line as an Fe^{2+} excitation (ground E_g doublet to A_{1g} singlet) is questioned since similar excitations appeared in rhodochrosite (at 1730 cm^{-1}) and dolomite (at 1755 cm^{-1}) which have either no iron detected (rhodochrosite) or only -6 atomic percent (dolomite), while the relative intensities in rhodochrosite and dolomite are approximately equal to those in siderite. As mentioned in the Popkov paper, if the 440 cm^{-1} line is considered to be a transition between spin-orbit exchange field split states (specifically from the lowest doublet to the uppermost), the frequency change should increase as the temperature is decreased through 38°K rather than decrease as the experimental observed change does. Also, the increase in frequency as the temperature is increased above the Néel temperature is not considered in this designation. Also in question is the statement referring again to the 440 cm^{-1} line:

> "The fact that this band does not vanish completely above the Néel temperature is apparently connected with conservation of short-range order at higher temperatures."[27]

While the possibility of magnetic short-range order at temperatures well above 38°K cannot be dismissed, it is thought that this spin-Raman transition could persist above the ordering temperature even with no short-range

order since the states are also separated by a spin-orbit energy difference.

In the other paper[28] concerned with siderite Raman excitations, the far infrared transmission spectrum of $FeCO_3$ is investigated for temperatures from 4.2°K to 70°K and in applied fields up to 90 kOe. At 4.2°K an excitation was observed at 112.5 cm^{-1} with parallel and perpendicular splitting factors of 6.6 and 0, respectively. This excitation and the 440 cm^{-1} and 1743 cm^{-1} Raman excitations are fit into an energy level splitting scheme of the Fe^{2+} ion.

The scheme initially follows Griffith by considering first a cubic splitting with a ground $^5T_2$ term. By use of the structural isomorphism to ^5P, the wavefunctions are expressed in terms of $|M_S, M_L>$ states with $M_S = \pm 2, \pm 1, 0$ and $M_L = \pm 1, 0$. For further splitting of the ground term, the single ion Hamiltonian,

$$H = R\lambda \bar{L} \cdot \bar{S} + R^2 \delta \left(L_z^2 - \frac{2}{3}\right) + JS_z \qquad (51)$$

is considered where λ, δ, and J are the spin-orbit, trigonal field, and Ising molecular field parameters, respectively. Both the exchange integral and the sum over surrounding spins are included in the molecular field parameter. R is an "orbital reduction factor" to be used as a parameter for fitting experimental data. Physically, R permits a variation of the orbital angular momentum from the exact value of L = 1. The trigonal field term is considered largest resulting in a singlet $^5A_1$ state and ground ^5E state if δ/λ is considered negative. In the limit of $\delta/\lambda \to -\infty$, the spin-orbit term will split the ^5E state into five equally spaced doubly degenerate states with M_J values of ± 1, 0, ± 1, ± 2, and ± 3 (in going from the

ground to uppermost states) and a single $|M_S, M_L>$ state corresponding to each M_J. However, in the interval $-\infty < \delta/\lambda < 0$, admixtures of $|M_S, M_L>$ states are considered for each M_J. For example, the first excited doublet is now split into the symmetric and antisymmetric pairs

$$\psi_1 = \alpha|1, -1> + \alpha|-1,1> + \varepsilon|0,0>$$
$$\psi_2 = a|1, -1> - a|-1,1> \qquad (52)$$

causing a splitting even when magnetic fields are not present. With the addition of an exchange or magnetic field, ψ_1 and ψ_2 are mixed resulting in

$$\psi_1' = \alpha|-1,1> + \beta|0,0> + \gamma|1,-1>$$
$$\psi_2' = -a|-1,1> + b|0,0> + c|1,-1> \qquad (53)$$

For the additional field splitting the exchange splitting, JS_z, is considered first followed by the Zeeman term $\beta\bar{H} \cdot (-R\bar{L}_i + 2\bar{S}_i)$.

The experimental excitations are considered by Prinz et al. to be between exchange split states which are assumed to have the same exchange parameter in the initial attempt. The 112.5 cm^{-1} infrared excitation is from the ground state ($\psi_g = |-2,1> + \varepsilon\{|-1,0> + |0,-1>\}$ to ψ_1'. The 440 cm^{-1} Raman excitation is from ψ_g to $|2,-1\rangle$, the lower exchange split state of the uppermost spin-orbit split doublet. The 1743 cm^{-1} Raman excitation is from ψ_g to $|-2,0>$, the lowest exchange split state of the trigonal field split singlet $^5A_1$. An analytic solution of the matrix of the Hamiltonian using these designations gives numerical values

for the R, λ, ζ and J parameters.

The designations of the Raman transitions is questioned for reasons similar to those given in the discussion of the paper by Popkov et al. The 1743 cm^{-1} line is not considered an Fe^{2+} excitation due to its strong relative intensity in rhodochrosite and dolomite. For the correct temperature dependence of the 440 cm^{-1} line, the upper state exchange splitting would have to be larger than the ground state splitting. However, as is stated by Prinz et al., the excited state exchange splitting is slightly smaller than the ground state. Also, in order to obtain simultaneously the correct parallel Zeeman splitting factor (6.6) and energy for the infrared transition, it was necessary to allow a different exchange constant for the first excited doublet (J_1 = 12.5 compared with J_0 = 18.5 for all other doublets).

Also in question is the relative order of the spin-orbit split levels (M_J = ±1,0, ±1,0, ±1, ±2, ±3), with ±1 lowest and ±3 uppermost. This is inconsistent with the expected inverted order of J levels for the more-than-half-filled Fe^{2+} 3d shell and does not correspond with the schemes of Kanamori and Griffith (as discussed in Chapter II). Griffith's levels are consistent with Kanamori's levels provided one takes into account the change in sign of $\bar{L}$ introduced by the structural isomorphism from $^5T_2$ to ^5P. If the signs of the M_L values in the ^5P configuration are changed, the M_J values will become ±3, ±2, ±1, 0, ±1 (going from lowest to highest energies in the spin-orbit split E_g state).

A question remains about the temperature dependence of the 112.5 cm^{-1} infrared excitation. From observation of the experimental results

of Prinz et al., the energy of the excitation did not change as the temperature was increased through T_N to 41°K and the excitation had vanished at 41°K. However, if this excitation is due to a transition from the ground state to the first excited doublet, a change in energy would be expected as the temperature increased through T_N due to removal of the exchange splitting. Also, above T_N a spin-orbit splitting between these two states still remains and it would be expected that the infrared excitation would persist above T_N.

Raman Excitations in CoF_2

Excitations in addition to the expected vibrational modes have been also observed[29] in CoF_2. CoF_2 is similar to $FeCO_3$ because it has an unquenched orbital angular momentum, and is antiferromagnetic with a Néel temperature of 37°K.

The additional excitations are best described with reference to the splitting scheme of Co^{2+} in $MgF_2:Co^{++}$[30] (as shown in Figure 16). The same scheme is used for Co^{2+} in CoF_2 for the crystal field and spin-orbit splittings. The effective Hamiltonian is

$$H_{eff} = -\Delta(L_z^2 - \frac{2}{3}) + \Gamma(L_x^2 - L_y^2) - \frac{3}{2}\lambda \bar{L}\cdot\bar{S} \qquad (54)$$

which operates on L_z, S_z states with S = 3/2 and L = 1. The terms in H_{eff} correspond to the cubic field, tetragonal field, and spin-orbit interaction respectively. The spin-orbit splitting results in a splitting of the $^4A_2$ singlet into two Γ_5^+ doublets as well as the splitting of the ^4E ground state into four Γ_5^+ doublets.

The Raman excitations in CoF_2 are classified in two groups. The

four low frequency lines (37, 169, 194, and 210 cm^{-1}) are from the two lowest doublets. Also four high frequency lines (783, 1089, 1218, and 1394 cm^{-1}) are from the four highest doublets. There was a frequency variation of all the excitations as the temperature was decreased through T_N as shown in Figure 17. The frequency shift ($\nu_4(2^oK) - \nu_1(85^oK)$) for the high frequency lines were reported as -19(783), +7(1089), -27(1218), and +4(1394).

Although it is acknowledged to be an approximation due to the orbital degeneracy, a spin Hamiltonian is used to fit experimental results involving the two lowest doublets. With the Hamiltonian[31]

$$H = \gamma (S_x^2 - S_y^2) + \delta S_z^2 \qquad (55)$$

acting only on the S = 3/2 manifold of four lowest states, a fit of the magnetic field splitting consistent with the 175 cm^{-1} spin-orbit splitting was possible. However, the temperature dependence of the frequencies was not explained and the Raman excitation energies did not approach the neutron values in the paramagnetic state above T_N.

For the four high frequency lines, Moch et al. followed the method Ishikawa and Moriya[32]: to derive the exciton spectrum from a self-consistent molecular field ground state of

$$H_{eff} + 2zS_zJ_{C_o-C_o} \langle S_z \rangle_o \ . \qquad (56)$$

The frequency shifts ($\nu_{AF} - \nu_{PARAMAGNETIC}$) predicted were +7(783), +27 (1084), +8 (1218) and +38(1394). The predicted values were all 20 to 35 cm^{-1} higher than the experimental values, and an explanation of the

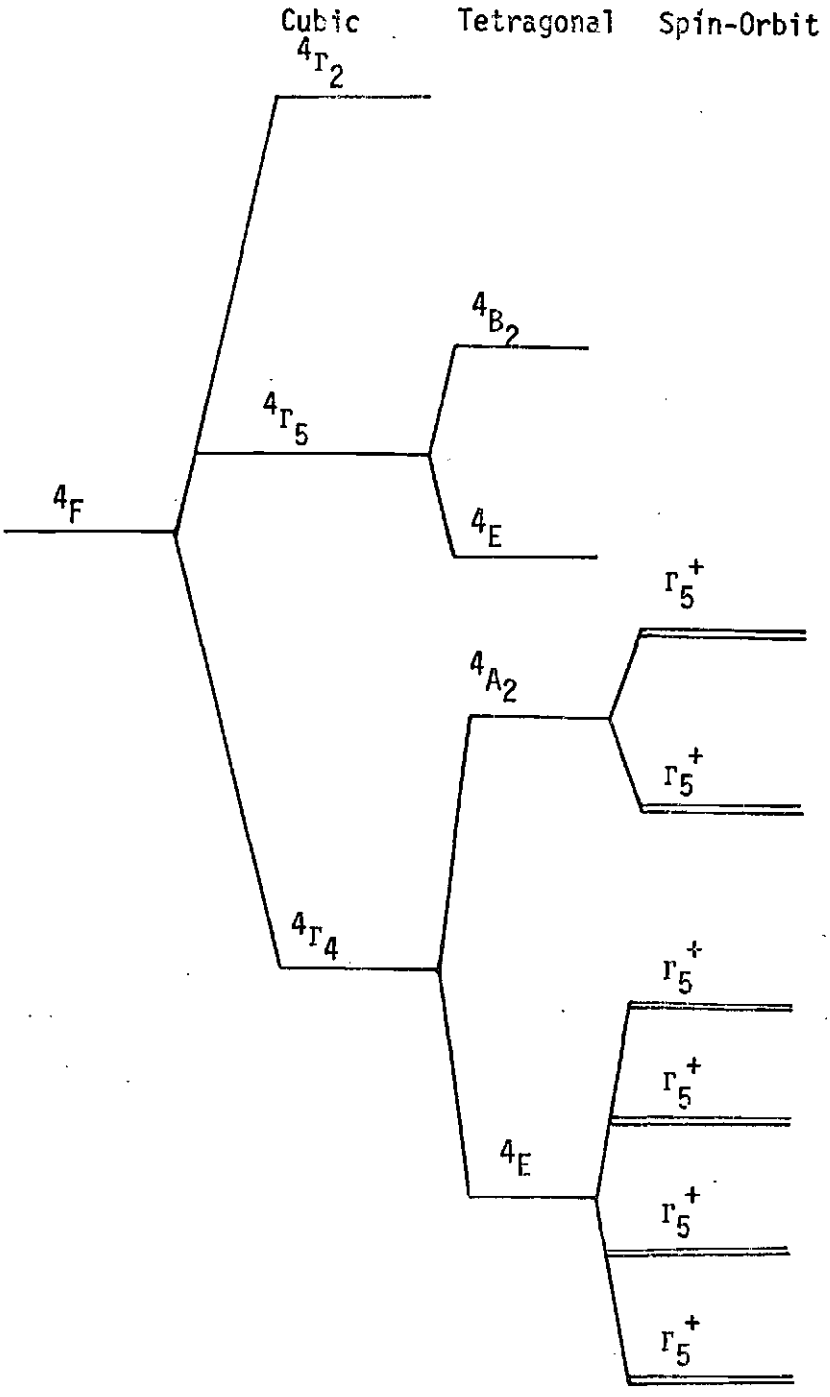

Figure 17. Crystal Field Splitting of Co^{2+} in $MgF_2:Co^{++}$.

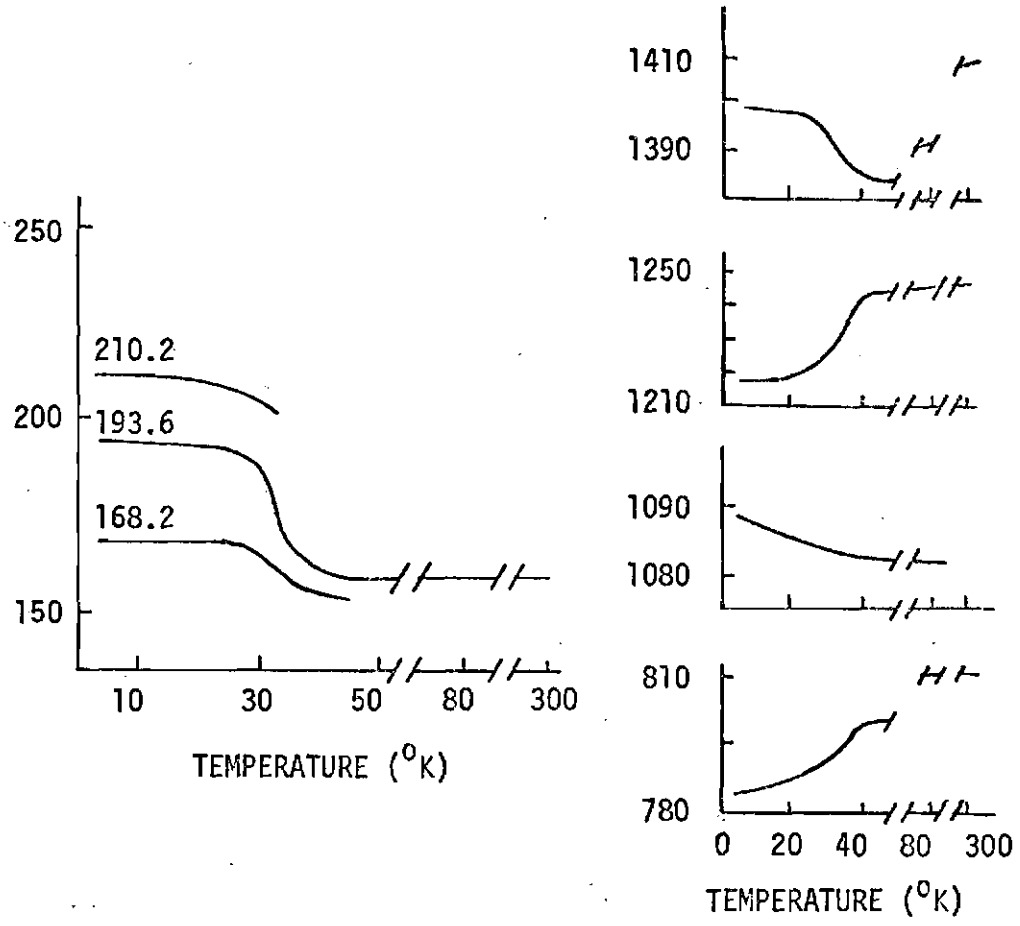

(a) Excitations generated by 2 lowest doublets.

(b) Excitations generated by 4 highest doublets.

Figure 18. Temperature Dependence of CoF_2 Raman Excitations (from Moch *et al.*[29])

temperature dependence was not presented.

Also of interest is the distinct frequency variation of two of the high frequency lines above the transition temperature. The 1394 cm^{-1} line decreases in frequency as the temperature is lowered from 1411 cm^{-1} at room temperature to 1387 cm^{-1} at $40^{o}K$ and then increases to 1394 cm^{-1} at $2^{o}K$. Also, the decrease of the 783 cm^{-1} line from 801 cm^{-1} at $80^{o}K$ to 792 cm^{-1} at $40^{o}K$ followed by a further sharp drop below T_N, is very similar to the temperature behavior of the 440 cm^{-1} line in $FeCO_3$.

Identification of Siderite Raman Excitations with Temperature Dependent Frequencies

The temperature dependent lines with frequencies of 440, 1175, and 1225 cm^{-1} at $6^{o}K$ are considered Fe^{2+} ion excitations between trigonal field and spin-orbit split states.

The most intense 440 cm^{-1} line is considered an Fe^{2+} excitation based on the relationship of Raman line intensities and iron concentrations in three different crystals: siderite, dolomite, and rhodochrosite. In siderite, 82% of the cations are iron and the 440 cm^{-1} intensity is the most intense. In dolomite 6% of the cations are iron impurities or the Fe^{2+} in dolomite is only 9% of the Fe^{2+} in siderite. The relative integrated intensity of the additional dolomite 504 cm^{-1} line is bracketed by values of 7.5 to 24.2% of the corresponding measurement of the 440 cm^{-1} line. (These measurements were made for spectra taken at $6^{o}K$ and the siderite percentage variation was due to measurements made on scans of different polarization components.). Hence the consistency of the decrease in intensity with the decrease of Fe^{2+} in dolomite indicates that the 440

cm^{-1} and 504 cm^{-1} lines are both due to the Fe^{2+} ion. Similarly, in rhodochrosite no iron impurity was detected and no Raman excitation around 500 cm^{-1} was observed. Although no Raman excitations were observed in dolomite to compare with the 1175 and 1225 cm^{-1} siderite lines, they may be present but too weak to observe. In siderite, the intensities of these higher lying lines are less than half that of the 440 cm^{-1} line.

These excitations can be fit into a crystal field splitting scheme which follows the Hamiltonian proposed by Griffith,

$$H = \frac{1}{4}\,\zeta\,\bar{L}\cdot\bar{S} + \delta\,(L_z^2 - \frac{2}{3}), \qquad (57)$$

which operates on $|M_S, M_L>$ states with $M_S = \pm 2, \pm 1$, and 0 and $M_L = \pm 1$, and 0. The resulting energy levels can best be presented as due to a trigonal field followed by a smaller spin-orbit splitting by plotting E/δ versus α, where $\alpha = \zeta/\delta$. When account is taken of the negative trigonal field parameter, the energy level splitting diagram (of $E/-\delta$ vs $-\alpha = \frac{\zeta}{-\delta}$) presented in Figure 18 is the result.

This splitting scheme is different from that proposed by Kanamori but it can be reduced to Kanamori's scheme. In Figure 18, the spin-orbit split levels from the E_g ground state are not equally split, the lower $M_J = 0$ levels are split and the upper A_{1g} trigonal singlet is split by the spin-orbit interaction. In Kanamori's scheme the spin-orbit split states are equally spaced, there is no splitting similar to the lower $M_J = 0$ separation, and spin-orbit splitting of the upper A_{1g} state is not mentioned. These differences are a consequence of the expression of

$$\overline{L}\cdot\overline{S} = L_+S_- + L_-S_+ + \frac{1}{2}L_zS_z \qquad (58)$$

when the matrix elements were evaluated in Griffith's scheme (where L_+, L_- signify orbital angular momentum raising and lowering operators, respectively.) The inclusion of $L_+S_- + L_-S_+$ results in the mixing of $|M_S, M_L>$ states which have the same M_J value. However, with the use of a spin-orbit term of the form

$$\sigma_z \langle L \rangle S_z ,$$

where $\sigma_z = \pm 1$, and $S_z = \pm 2, \pm 1$, and 0, Kanamori is using only the L_zS_z term of $\overline{L}\cdot\overline{S}$. If only this term is used in Griffith's Hamiltonian, five equally spaced spin-orbit split ground states and an unsplit A_{1g} state would persist. For complete correspondence with Kanamori, the M_J (^5P) values of Figure 18 should be changed to 3, 2, 1, 0, 1 for the increasing levels in the ground state. The designations ^5P in Figure 18 were a consequence of the change $\overline{L} \rightarrow -\overline{L}$ introduced by the isomorphism $^5T_2 \rightarrow {}^5P$ in the ground cubic state. The $M_J(^5T_2)$ values are listed in the second column in Figure 18. These numbers signify the real orbital angular momentum values, and further descriptions of this scheme will refer to these M_J ($^5T_2$) values.

In most reasonable designations of the Raman excitations to the levels in Figure 18 are as follows:

(a) 460 cm^{-1} From ground state ($M_J = 3$) to uppermost E_g doublet ($M_J = 1$)

(b) 1175 cm^{-1} From ground state to lowest A_{1g} doublet ($M_J = 2$)

(c) 1255 cm^{-1} From ground state to either of the two highest A_{1g} levels ($M_J = 0$ cr $M_J = 1$)

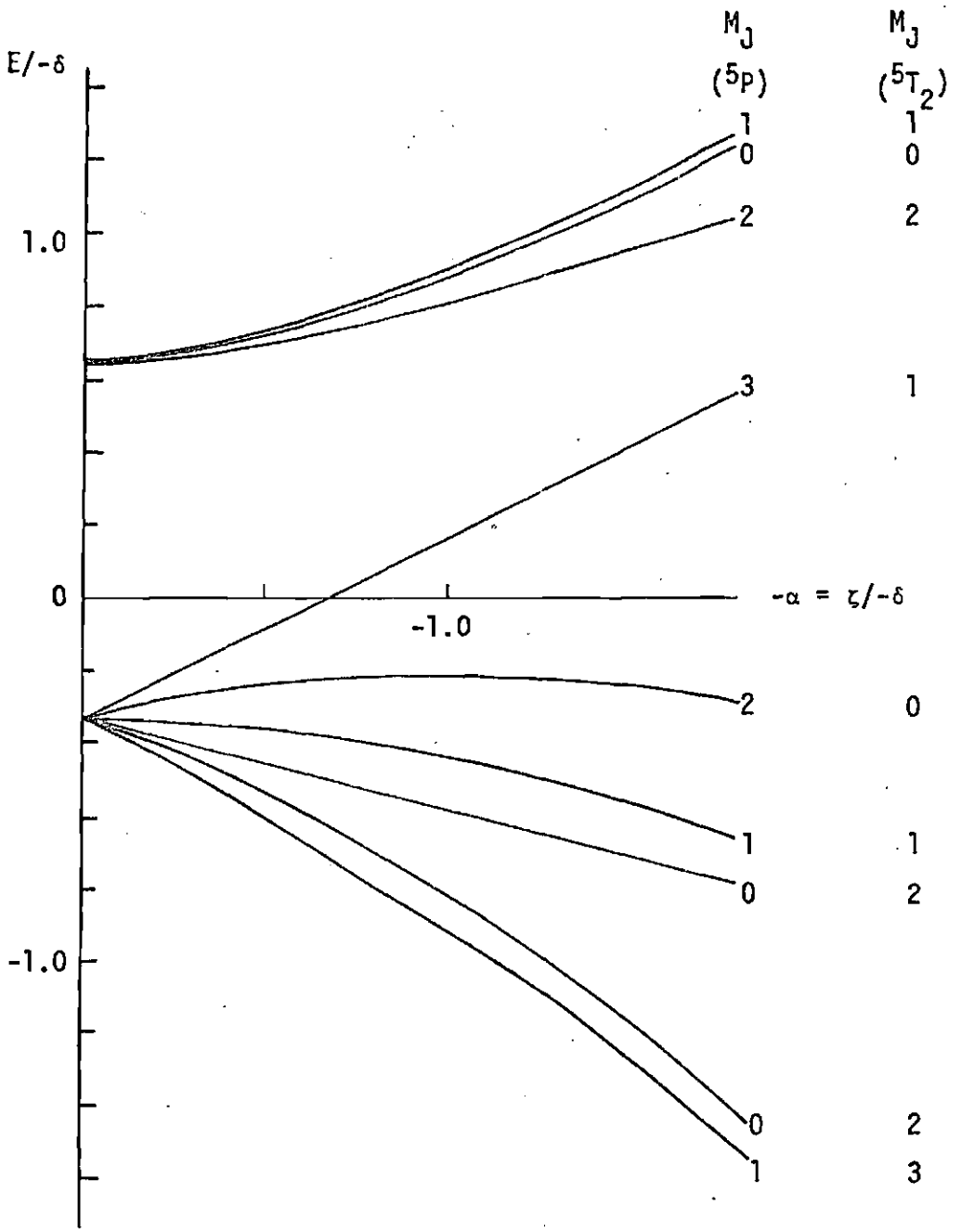

Figure 19. Trigonal and Spin-Orbit Splitting of Fe^{2+} (following Griffith).

The values presented here are the energies at $T_N = 38^oK$ prior to the effects of the long range antiferromagnetic ordering.

The next step is to explain the energy shift of these excitations from 38^oK to 6^oK, by the use of an appropriate Hamiltonian for the exchange interaction. There are two initial choices for the exchange Hamilton

$$(a)\quad H_{ex} = -J \sum_j S_i^z S_j^z, \quad \text{and} \tag{59}$$

$$(b)\quad H_{ex} = -J \sum_j J_i^z J_j^z \tag{60}$$

where S_i^z, J_i^z, and J refer to the M_S, M_J, and exchange parameter values, respectively. The problem with the S^zS^z Hamiltonian, (a), is that no account was taken of the unquenched orbital angular momentum in this Heisenberg form. It also cannot be directly applied to the levels of Figure 18 since they do not correspond to pure M_S states. However, when spin-orbit mixing is not considered, these E_g levels, starting from the ground state, have M_S values of ±2, ±1, 0, ±1, ±2 (similar to the Kanamori scheme). When the S^zS^z Hamiltonian is applied to these M_S states, the ground state energy level is not lowered any more than any of the upper levels and hence a decrease in energy splitting with decreasing temperature is not predicted. Although the J^zJ^z Hamiltonian, (b), considers the orbital angular momentum by adding it directly to the spin, its energy decrease is not predicted since the ground state ($M_J = 3$) will have a larger splitting than any of the higher states.

Discussion of the Interpretation of the Temperature Dependent Frequency Excitations

The designation of the 460 cm^{-1} energy at 38°K as a transition from the ground spin-orbit split E_g doublet indicates that the spin-orbit split levels are not equally separated in energy. If the 87 cm^{-1} separation between the ground and first excited doublets as reported by Wrege, were repeated between all states in the manifold, the energy from the ground to uppermost state could be 348 cm^{-1}. Also, the 460 cm^{-1} observation is not consistent with Kanamori's prediction that the spin-orbit levels would be equally split.

The form for the spin-orbit interaction in the Griffith Hamiltonian ($\frac{1}{4}\zeta \vec{L}\cdot\vec{S}$) may need further refinement. The general form for the spin-orbit interaction of an electron in a crystal is

$$\frac{h}{4m^2c^2}\,(\nabla V \times \vec{P} \cdot \vec{S}),^{33}$$

where V is the Coulomb potential of the electron due to the atomic nucleus and the surrounding crystal field. This expression will reduce to the $\vec{L}\cdot\vec{S}$ form only when the potential is spherically symmetric. In the case of the outer d electrons of Fe^{2+} in the trigonal crystal field, this reduction does not follow and the magnitude of the relative spin-orbit splittings predicted by the Griffith Hamiltonian may be questioned. However, the number of spin-orbit split levels and their symmetries are not questioned since these were determined from a reduction of

$$\Gamma(L) \times \Gamma(S)$$

where $\Gamma(L)$ are representations of orbital states already split by the

trigonal field and the $\Gamma(S)$ are the representations of the spin states expressed in the D_{3d} symmetry.

After these designations have been made, more observations and comparisons may be made. In both $FeCO_3$ and CoF_2 Raman transitions to trigonal spin-orbit split levels were observed (including transitions to spin-orbit split singlet levels in both cases). Also in these two crystals there was further splitting below the Néel temperature due to magnetic ordering. There were also Raman transitions in MgF_2: Co^{2+} to the same levels as in CoF_2[29] although there was no additional splitting due to ordering. The Ca^{2+} ion would also be expected to be split by cubic and trigonal fields in $CaCO_3$, but no additional Raman excitations were observed. Since the Ca^{2+} ion has a closed $3p^6$ shell with S = 0, the observation from the results of these four samples is that for Raman transitions to occur between ion split levels, there must be an unpaired spin associated with these levels and that coupling of the light with the spins is the mechanism involved. Although electronic Raman transitions were observed between ionic states in $PrCl_3$ and $LaCl_3$ (by Hougen and Singh[37]) and in $CeCl_3$ (by Kiel[38]) the significance of the spin was only found in the paper by Shen and Bloembergen.[19] The persistance of excitations to ionic states in the paramagnetic phase in $FeCO_3$ and CoF_2 gives further support to the spin-Raman concept.

An attempt to account for the unquenched orbital angular momentum in the exchange interaction has been attempted by Elliott and Thorpe.[34] The approach was to start with the Heisenberg form,

$$W(i,j) + 2J(i,j)\,[\bar{S}_i \cdot \bar{S}_j + \tfrac{1}{4}] \qquad (61)$$

with the Coulomb, W(i,j), and exchange interactions expressed in terms of tensor operators which operate on single-electron states. The problem is then to find an effective Hamiltonian in a pseudospin representation which represents the same interaction in the ground state of the ions in a crystal field with a spin-orbit interaction. With the use of this technique, the predicted results were closer than those of the Heisenberg form but still did not predict the experimental results. As far as can be determined from contact with these authors and from literature surveys, no further theoretical work has been done on the problem of exchange interaction with unquenched orbital angular momentum.[35] Thus, the problem of explaining the temperature dependence of these Co^{2+} and Fe^{2+} related lines will probably only be solved when a correct formulation of the unquenched orbital angular momentum problem is found. A solution to this problem should result in a better understanding of magnetic ions in crystals.

Identification of Siderite Raman Excitations with Temperature Independent Frequencies

By comparison of Raman spectra, infrared spectra, and impurity analyses of siderite, dolomite, and rhodochrosite, the 747 cm^{-1} and 1740 cm^{-1} Raman excitations in siderite may be identified.

The 747 cm^{-1} excitation is identified as the infrared 747 cm^{-1} $(\nu_{15})E_u$ mode becoming Raman active due to loss of inversion symmetry as a result of Fe^{2+} ordering as the temperature is decreased. (It is not construed to be the $\nu_{11}(E_g)$ mode as reported by Popkov et al.) The increase of the integrated intensity (as presented in Figure 14) with

decreasing temperature is consistent with this identification. The physical picture for this behavior is that at room temperature (the highest temperature at which spectra were taken and evidence of a Raman 747 cm^{-1} line was observed), there is a small amount of short range ordering of the Fe^{2+} ions in clusters. In the cluster, the ordering distorts the symmetry of the unit cell from D_{3d}^6 to another symmetry which favors the ν_{15} (E_u) mode. For this odd parity mode to exist, the new symmetry cannot include a center of inversion symmetry.[36] As the temperature is lowered, the size of the ordered clusters increases and larger percentage of the incident laser light induces Raman transitions in the distorted symmetry. Also consistent with this picture is the observation that the integrated intensity remains relatively constant below 30^oK where all ordering is completed.

Further evidence for this identification of the 747 cm^{-1} line was obtained by considering experimental results in dolomite and rhodochrosite. The additional 728 cm^{-1} Raman line in dolomite $CaMg(CO_3)_2$ can also be identified as the 729 cm^{-1} $(\nu_{15})E_u$ mode observed in the dolomite infrared spectra. The explanation that this 728 cm^{-1} Raman line was substantially intense at room temperature and that its intensity did not increase as the temperature was lowered, is that the distortion in dolomite is due to the lack of symmetry due to the iron ion impurity and not to iron ordering. The concentration of iron (6% cation concentration) is too small for ordering but large enough to distort the D_{3d}^6 symmetry. Also, the infrared 728 cm^{-1} $(\nu_{15})E_u$ mode in rhodochrosite was not observed in the rhodochrosite Raman spectra at any temperature. No distortion would be expected since the impurity concentration was very low and no iron was detected.

The 1740 cm^{-1} Raman excitation in siderite is identified as an overtone of the experimentally observed 870 cm^{-1} (ν_7) A_{2u} infrared mode. In support of this identification is the observation that a similar identification can be made from the dolomite and rhodochrosite spectra. In dolomite the 1760 cm^{-1} Raman excitation is due to the 880 cm^{-1} infrared overtone. In rhodochrosite, the 1732 cm^{-1} line is due to the 866 cm^{-1} infrared overtone. It is not considered an Fe^{2+} transition from the ground E_g spin-orbit split state to the A_{1g} singlet as proposed by Popkov et al. and used in the calculations of Prinz et al. The 1760 cm^{-1} dolomite and 1732 cm^{-1} rhodochrosite lines had the same relative intensity as the 1740 cm^{-1} siderite line but there was only 6% Fe^{2+} in dolomite and no iron detected in rhodochrosite. Hence these 1700 cm^{-1} Raman lines would not be due to Fe^{2+} excitations.

Unidentified Siderite Raman Excitations

Of the additional Raman excitations, the 1495 cm^{-1} and 870 cm^{-1} lines have not been identified.

The 1495 cm^{-1} line is most intense at $6^{o}K$ and its intensity decreases as the temperature is increased. One possible explanation is an overtone of the 747 cm^{-1} (ν_{15}) E_u mode. However, a similar identification was not possible in dolomite or rhodochrosite since no excitations at twice the ν_{15} (E_u) frequencies were observed in the Raman spectra. If this possible explanation were correct, the overtone in dolomite would be more likely than in rhodochrosite since the ν_{15} (E_u) mode itself was Raman active in dolomite as in siderite. Another possibility is an Fe^{2+} ion excitation to the third A_{1g} singlet level. The increasing intensity with decreasing

temperature favors this possibility but constant frequency through the transition temperature does not. Also, the 1495 cm^{-1} energy would be too large to be consistent with the splittings predicted by Griffith's Hamiltonian and the previous identifications of the 440, 1175, and 1225 cm^{-1} excitations.

A possible explanation of the 870 cm^{-1} excitation is that it is the 870 cm^{-1} (ν_7) A_{2u} infrared mode becoming Raman-active due to ordering induced distortions as the temperature is lowered. Although a Raman line was not observed in dolomite corresponding to the 880 cm^{-1} (ν_7) A_{2u} infrared mode, dolomite is expected to have distortions based on identification of the ν_{11}(Eg) mode. However, the distortions in dolomite may be different from those in siderite so that both modes (ν_7 and ν_{11}) would not be expected to be Raman active in dolomite.

Effect of Parameter Variation on Trigonal Distortion in Siderite

Analysis of neutron diffraction results performed on siderite at the Georgia Tech Research Reactor revealed changes in the rhombohedral lattice parameters (a_o and α in Figure 1) as the temperature was decreased.[39] The results of this analysis are presented in Figure 20. It is observed that the largest change in both a_o and α is between room temperature and liquid nitrogen temperature (78^oK).

By relating these lattice parameters to the trigonal distortion from cubic symmetry, it is possible to predict energy shifts for transitions between spin-orbit trigonal field split levels of the Fe^{2+} ion in siderite. Specific interest was in the 440 cm^{-1} Raman excitation as it changed in frequency from 525 cm^{-1} (at room temperature) to 468 cm^{-1} (at 78^oK).

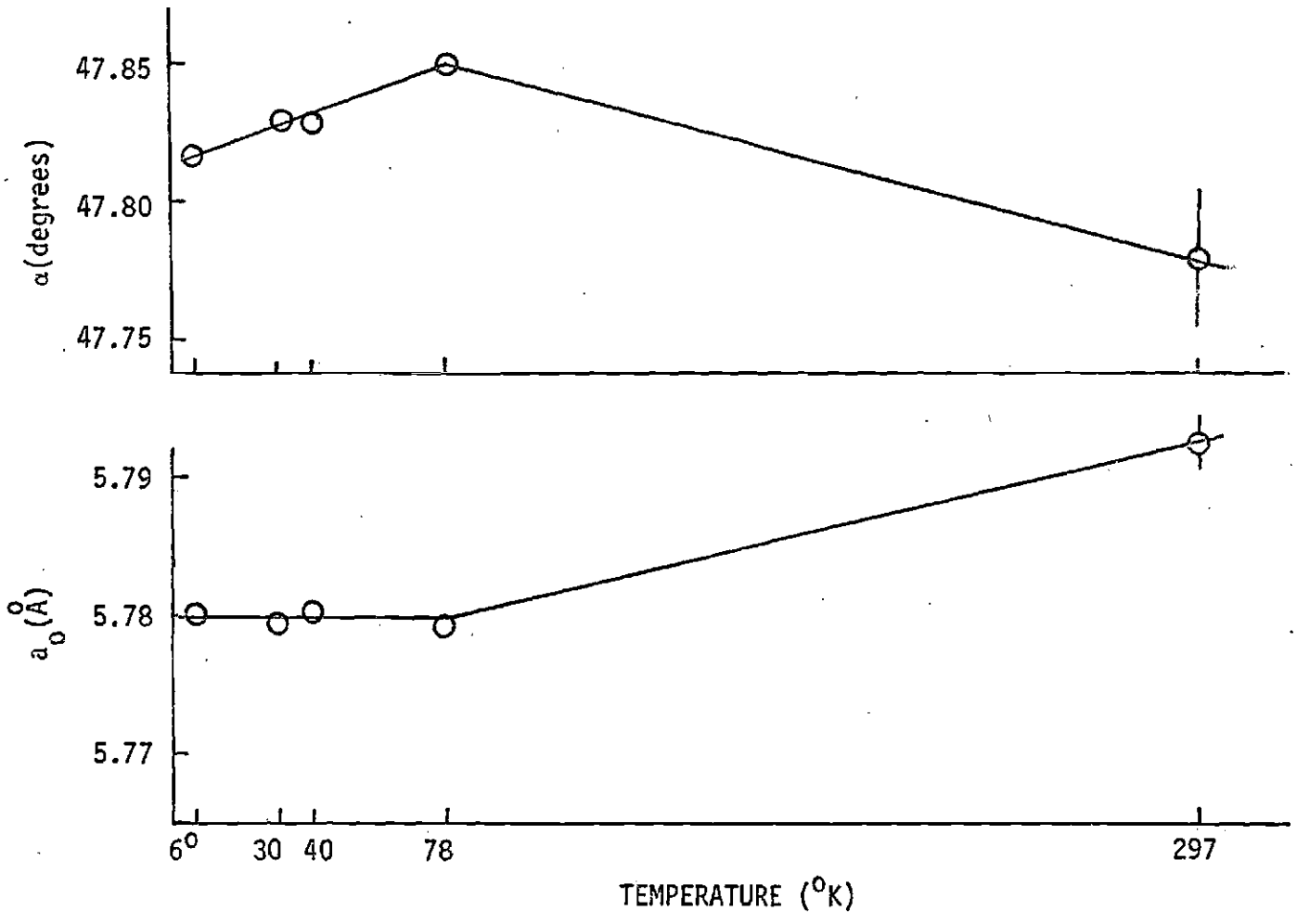

Figure 20. Siderite Lattice Parameter Variation with Temperature.

A calculation was performed which combined the Griffith Hamiltonian[26] and the point-charge method[40] of determination of crystal field potentials. The δ variable in the Griffith Hamiltonian, $H = \frac{1}{4}\rho\,\overline{L}\cdot\overline{S} + \delta\,(L_z^2 - \frac{2}{3})$, is a measure if the trigonal distortion of the crystal field potential at the Fe^{2+} site from cubic symmetry. The potential is assumed due to the six nearest oxygen atoms. δ can be expressed in terms of the iron-oxygen distance and the angle the iron to oxygen direction makes with the c-axis (to be called d and θ, respectively). d and θ can then be related to the temperatures dependent a_0 and α. By comparing coefficients of a point charge calculation[39] for this symmetry it is found that δ (and hence $\omega = \frac{\delta}{\rho}$) is proportional to $\frac{1}{d^3}(3\cos^2\theta - 1)$.

The results of this calculation are presented in the table below in terms of percent changes of the indicated quantities between room temperature and 78^0K.

a_0	α	ω	ΔE	$\Delta E_{observed}$
-.27%	.15%	-.68%	-.033%	-8.35%

The ΔE represents the energy shift from the ground Eg doublet to the uppermost Eg doublet. The ΔE observed indicates the change in the 440 cm^{-1} Raman excitation. The energy change predicted by this calculation is the correct direction but the magnitude is too small by a factor of 250.

It is still possible that the change in energy of the 400 cm^{-1} line above (as well as the 1175 and 1225 cm^{-1} lines) may be due to variation of trigonality with temperature. Due to the non-spherical environment

the $\overline{L} \cdot \overline{S}$ form for the spin-orbit energy may not be correct. Another form derived from the more general expression,

$$\frac{h}{4m^2c^2} (\nabla V \times \overline{P} \cdot \overline{S}) ,$$

which considers a trigonal V with full spherical coordinate dependence, (r, θ, ϕ), may be more sensitive to changes in trigonal distortion.

Investigation of Soft Modes at Brillouin Zone Boundary by Neutron Diffraction Experiment

Another possible explanation of the siderite Raman 440 cm^{-1} excitation was that it may be due to an overtone of the $Eg(\nu_{12})$ 287 cm^{-1} Raman active mode (see Figure 8) at the Brillouin zone boundary. In spite of the limitation that the photon momentum transfer is near zone center for Raman scattering, two phonon excitations are possible at zone boundary with the wavevectors in opposite directions. Investigation of this mode at zone boundary indicates that an overtone could occur at symmetry points Z, A, or D of the rhombohedral Brillouin zone (see Figure 20).

The neutron diffraction experiment proposed was to look for the single phonon mode at half the Raman room temperature energy($\frac{1}{2}$ (525 cm^{-1}) = 262 cm^{-1} = 7.85 THz.) at the mentioned boundary points. Both the transverse and longitudinal modes would be investigated. If the correct energy occurs in a mode at any of these points, the energy for that mode and point would be observed at liquid nitrogen temperature for comparison with the Raman value (468 cm^{-1} = 234 cm^{-1} = 7.02 THz.). If neutron peaks at these energies were observed, then a magnetically coupled soft mode explanation would be possible.

The experiment was performed at the triple axis spectrometers at the High Flux Isotope Reactor at Oak Ridge National Laboratory. The results are summarized in Table 6. The peak energies are given for the longitudinal optic (LO) and transverse optic (TO) modes of each symmetry point. The τ, q, and Q values correspond to the reciprocal lattice point, the momentum transfer to the zone boundary point, and the total neutron momentum, respectively, for the particular mode investigated. The momentum vector components are given with respect to hexagonal axes. The energy was varied in steps of 0.2 THz. for the scans.

The conclusion was that none of the energies of the modes investigated corresponded to half the Raman energy (262 cm^{-1}). Thus the 525 cm^{-1} Raman line was probably not a two phonon excitation that became soft as the temperature decreased.

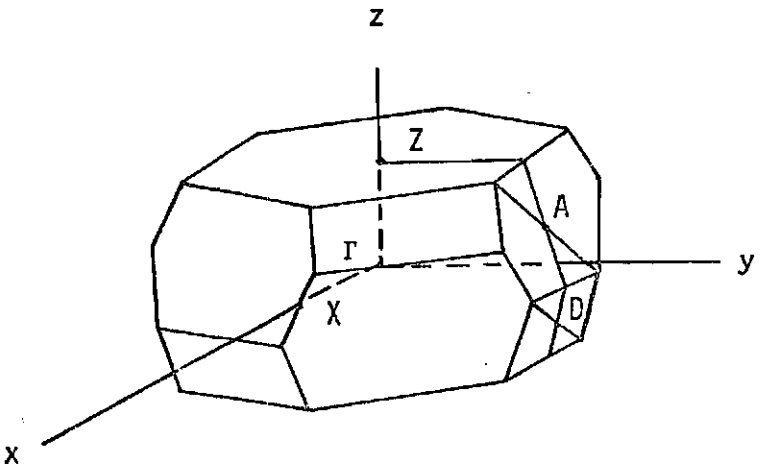

Figure 21. The First Brillouin Zone for the Rhombohedral Lattice.

Table 6. Summary of Experimental Values of Neutron Diffraction Investigation of Zone Boundary Modes in Siderite

Symmetry Point	Mode Favored	τ	q	Q	Energy (TH_z)	Energy (cm^{-1})	Peak Counts	Background Counts
A	LO	$(3,0,\bar{3})$	$(.5,0,.\bar{5})$	$(3.5,0,\overline{3.5})$	7.2	240	274	72
	TO	$(1,0,14)$	$(.5,0,.\bar{5})$	$(1.5,0,13.5)$	7.2	240	60	30
D	TO	$(2,0,\overline{13})$	$(.5,0,1)$	$(2.5,0,\overline{12})$	7.2	240	25	15
Z	TO	$(3,0,0)$	$(0,0,1.5)$	$(3,0,1.5)$	6.3	210	86	35
	LO	$(0,0,12)$	$(0,0,1.5)$	$(0,0,13.5)$	5.7	190	235	30

CHAPTER V

CONCLUSIONS

The three Raman excitations with temperature dependent frequencies (440, 1175, and 1225 cm^{-1} at $6^{o}K$) are considered transitions between trigonal crystal field and spin-orbit split levels of the Fe^{2+} ion in siderite. Sharp frequency shifts immediately below $38^{o}K$ are consistent with the previous observations that a magnetic transition occurs at $38^{o}K$. These excitations indicate a splitting of approximately 1000 cm^{-1} between the E_g and A_{1g} trigonal states (not including the spin-orbit splitting) as predicted by Kanamori. However, the 440 cm^{-1} energy indicates the spin-orbit split levels of the ground E_g state are not equally spaced as proposed by Kanamori but follow a Hamiltonian as proposed by Griffith. The situation that the temperature dependence of these excitations cannot be explained by the Heisenberg form of the exchange interaction is consistent with the condition that the orbital angular momentum is unquenched.

The constant frequency 747 cm^{-1} Raman excitation is considered the infrared $(\nu_{15})E_u$ mode which becomes Raman active due to loss of inversion symmetry as a result of Fe^{2+} ion ordering as the temperature is decreased. This indicates that short range order may persist up to $297^{o}K$ (room temperature).

CHAPTER VI

RECOMMENDATIONS

There are other experiments which could provide more information about the magnetic behavior of siderite. Infrared siderite spectra taken at temperatures varying from liquid helium temperature to room temperature from 300 cm^{-1} to 1600 cm^{-1} could check for a Raman modes becoming infrared active due to ordering distortions upon cooling. Also, excitations to other spin-orbit split E_g and A_{1g} levels as well as to the levels reached by the Raman experiment could be expected. Neutron diffraction experiments could be performed to check for observation and dispersion of the Raman excitations with temperature dependent frequencies.

A detailed group theory analysis could be attempted to determine Hamiltonians for the exchange interaction with unquenched orbital angular momentum and for the spin-orbit interaction in the non-spherical crystal field potential. Such an investigation would be particularly useful since temperature varying Raman frequencies above the transition temperature and unexplained frequency shifts below T_N are present in both CoF_2 and $FeCO_3$.

BIBLIOGRAPHY

1. J. H. Van Vleck, The Theory of Electric and Magnetic Susceptibilities, Oxford University Press, Clarendon (1932).

2. J. C. Bjorken and S. D. Drell, Relativistic Quantum Mechanics, McGraw-Hill, Inc., (1964), p. 51.

3. R. J. Elliott, The Physical Review, 96, 280 (1954).

4. R. J. Elliott and M. F. Thorpe, Journal of Applied Physics, 39, 802 (1968).

5. R. W. G. Wychoff, Crystal Structures, Vol. II, Interscience, N.Y. (1964), p. 362.

6. R. A. Alikhanov, Soviet Physics - JETP, 9, 1204 (1959).

7. I. S. Jacobs, Journal of Applied Physics, 34, 1106 (1963).

8. D. W. Forester and N. C. Koon, Journal of Applied Physics, 40, 1316 (1969).

9. N. C. Koon, Ph. D. Dissertation, Georgia Institute of Technology, 1969 (unpublished).

10. J. Kanamori, Progress of Theoretical Physics, 20, 890 (1958).

11. K. Ono and A. Ito, Journal of the Physical Society of Japan, 19, 899 (1964).

12. C. E. Johnson, W. Marshall, and G. J. Perlow, The Physical Review, 126, 1503 (1962).

13. A. Okiji and J. Kanamori, Journal of the Physical Society of Japan, 19, 908 (1964).

14. D. E. Wrege, S. Spooner, and H. A. Gersch, in AIP Conference Proceedings, Magnetism and Materials, No. 5, 1971, ed. by C. D. Graham and J. J. Rhyne, AIP, New York (1972), p. 1334.

15. G. A. Prinz and D. W. Forester, abstracted in AIP Conference Proceedings, Magnetism and Magnetic Materials, No. 5, 1971, ed. C. D. Graham and J. J. Rhyne, AIP, New York (1972), p. 279.

16. S. I. Mizushima, in Handbuch Der Physik, Vol. XXVI, ed. S. Flugge and P. J. Wijn, Springer-Verlag, Berlin (1958), p. 196.

17. M. M. Suschinskii, Raman Spectra of Molecules and Crystals, Israel Program for Scientific Translations Ltd., New York (1972), p. 64.

18. Y. R. Shen, Journal of Applied Physics, 32, 1490 (1967).

19. Y. R. Shen and N. Bloembergen, The Physical Review, 143, 372 (1966).

20. S. Bhagavantum and T. Venkatarayudu, Theory of Groups and its Application to Physical Problems, Academic Press (1969), p. 140.

21. M. Tinkham, Group Theory and Quamtum Mechanics, McGraw-Hill, Inc., New York (1964), p. 39.

22. J. Nakagawa and J. L. Walter, The Journal of Chemical Physics, 51, 1389 (1969).

23. R. Loudon, Advances in Physics, 13, 423 (1964).

24. F. G. Bass and M. I. Kaganov, Soviet Physics - JETP, 10, 986 (1960).

25. R. J. Elliott and R. Loudon, Physics Letters, 3, 189 (1963).

26. J. S. Griffith, The Theory of Transition Metal Ions, Cambridge University Press, Cambridge (1961).

27. Y. A. Popkov, V. V. Eremenko, V. I. Fomin, and A. P. Mokhir, Soviet Physics - Solid State, 14, 1985 (1973).

28. G. A. Prinz, D. W. Forester, and J. L. Lewis, The Physical Review, B8, 2155 (1973).

29. P. Moch, J. P. Gosso, and C. Dugautier, in Proceedings of the Second International Conference on Light Scattering in Solids, 1971, ed. M. Balkanski, Flammarion, Paris, p. 138.

30. H. M. Gladney, The Physical Review, 146, 253 (1966).

31. M. E. Lines, The Physical Review, 137, A982 (1965).

32. A. Ishikawa and T. Moriya, Journal of the Physical Society of Japan, 30, 117 (1971).

33. R. J. Elliott, The Physical Review, 96, 280 (1954).

34. R. J. Elliott and M. F. Thorpe, Journal of Applied Physics, 39, 802 (1968).

35. M. F. Thorpe, private communication.

36. P. A. Fleury and J. M. Worlock, The Physical Review, 174, 613 (1968).

37. J. T. Hougen and S. Singh, Proceedings of the Royal Society (London), A277, 193 (1964).

38. A. Kiel, in Proceedings of the International Conference on Light Scattering Spectra of Solids, 1969, ed. G. B. Wright, Spring-Verlag, New York, p. 245.

39. Data taken by R. Altman and D. B. Langille. Analysis performed by R. Medina.

40. M. T. Hutchings, Solid State Physics, 16, 227 (1964).

VITA

Douglas Bruce Langille was born in New York, New York on November 18, 1944. He was graduated from DuPont High School in Jacksonville, Florida in 1962. He received both the Bachelor of Science degree in Physics (in 1966) and the Master of Science degree in Physics (in 1968) from the Georgia Institute of Technology.

As a graduate student, he received an NDEA Title IV Fellowship, a teaching assistantship from the Georgia Tech School of Physics, and a fellowship from the United States Steel Corporation. He also was employed as a graduate research assistant by the Crystal Physics Branch of the Georgia Tech Engineering Experiment Station and as an instructor by DeKalb Community College. He is a member of Tau Beta Pi, Sigma Pi Sigma, and other honorary societies.

In 1969 he was married to Charlotte Lucy Branscombe and they have one daughter, Catherine Marie.